

1 **Assimilation of Himawari-8 Imager Radiance Data with the WRF-3DVAR**

2 **system for the prediction of Typhoon Soudelor**

3 **Dongmei Xu^{1,2,3}, Feifei Shen^{1,2,3*}, Jinzhong Min¹, Hong Li⁴, Aiqing Shu¹**

4
5 *1. The Key Laboratory of Meteorological Disaster, Ministry of Education*
6 *(KLME)/Joint International Research Laboratory of Climate and Environment*
7 *Change (ILCEC)/Collaborative Innovation Center on Forecast and Evaluation of*
8 *Meteorological Disasters (CIC-FEMD), Nanjing University of Information Science &*
9 *Technology, Nanjing 210044, China*

10 *2. Heavy Rain and Drought-Flood Disasters in Plateau and Basin Key Laboratory*
11 *of Sichuan Province, Chengdu, China*

12 *3. The Institute of Atmospheric Environment, China Meteorological Administration,*
13 *Shenyang 110000, China*

14 *4. Shanghai Typhoon Institute, China Meteorological Administration, Shanghai*
15 *200030, China*

16

17

18

19 **Abstract**

20 Himawari-8 is a new generation geostationary meteorological satellite launched
21 by Japan Meteorological Agency (~~JMA~~). It carries the Advanced Himawari Imager
22 (AHI) onboard, which can continuously monitor high-impact weather events with
23 high frequency space and time. The assimilation of AHI radiance data was
24 implemented with the three-dimensional variational data assimilation system of
25 Weather Research and Forecasting model (~~WRF-3DVAR~~) for the analysis and
26 prediction of Typhoon Soudelor (2015) in the Pacific Typhoon season. The effective
27 assimilation of AHI radiance data in improving the forecast of the tropical cyclone
28 during its rapid intensification has been realized. The results show that after
29 assimilating the AHI radiance data under clear sky conditions, the typhoon position in
30 the background field of the model ~~is~~was effectively corrected compared with the
31 control experiment without AHI radiance data assimilation. It is found that the
32 assimilation of AHI radiance data is able to improve the analyses of the water vapor
33 and wind in typhoon inner-core region. The analyses and forecasts of the minimum
34 sea level pressure, the maximum surface wind, and the track of the typhoon are
35 further improved.

36 **Key words:** Weather Research and Forecasting model; Three-Dimensional
37 Variational Data Assimilation; AHI Radiance Data; Typhoon

38

39 **1. Introduction**

40 In recent years, although researchers have made great progress in the field of
41 numerical weather prediction (NWP), the huge challenges are encountered in the
42 accurate forecasts of tropical cyclones (TCs) with rapid intensifications (DeMaria et
43 al., 2014). The predictability of these TCs is limited because it entails complex
44 multi-scale dynamic interactions (Minamide and Zhang 2018). These interactions
45 include environmental airflows, TC vortex interactions, atmosphere-ocean
46 interactions, and the effects of mesoscale and micro-convective scale, together with
47 the microphysics and atmospheric radiation. In order to attain a better initial condition
48 and improve the accuracy of the forecast, data assimilation seeks to fully utilize the
49 observations. The life span of most TCs is over the ocean where conventional
50 observations are relatively insufficient compared to the land. Therefore, by analyzing
51 observed data from satellites and planes over the ocean, it is crucial to adopt effective
52 data assimilation (DA) methods to improve the analysis and forecast of TCs.

53 With the rapid development of atmospheric radiative transfer model, many
54 numerical weather prediction centers have adopted variational DA method to
55 assimilate a variety of radiance data from different satellite observation instruments
56 (Bauer et al., 2011; Buehner et al., 2016; Derber et al., 1998; Hilton et al., 2009;
57 Kazumori et al., 2014; McNally et al., 2006; Prunet et al., 2000; Pennie, 2010). These
58 data can take up 90% of all data used in global DA system and can improve the
59 accuracy of the numerical model results strikingly (Bauer et al., 2010). Some

带格式的: 字体颜色: 红色

带格式的: 字体: (中文) 黑体, 小四,
字体颜色: 文字 1

60 researches demonstrated that in global model, satellite radiance DA makes more
61 contribution to improving the accuracy of the numerical model results than
62 conventional observation DA does (Zapotoeny et al., 2007, Yan et al., 2010; Geer et
63 al., 2017)~~Some researches demonstrated that in global model, satellite radiance DA~~
64 ~~makes more contribution to improving the accuracy of the numerical model results~~
65 ~~than conventional observation DA does (Zapotoeny et al., 2007).~~

66 Generally speaking, radiance data are derived from microwave and infrared
67 detecting instruments, which are from polar-orbit satellites and geostationary satellites,
68 respectively. Polar-orbit satellites cover the sphere of all the earth, thereby suitable for
69 global NWP models (Jung et al., 2008). Besides, they have finer resolutions compared
70 to geostationary satellites (Li et al., 2017; Shen et al., 2015; Xu et al., 2013). However,
71 it is highlighted that they are not able to generate continuous observations for a fixed
72 regional area and so may miss rapidly intensified TCs or storms.~~However, it is~~
73 ~~highlighted that they are not able to perform continuous monitoring objects as some~~
74 ~~rapidly intensified TCs or storms over a fixed area, thus leaving out some rapidly~~
75 ~~intensified TCs or storms.~~ On the contrary, because geostationary satellites ~~have a~~
76 ~~fixed location related to the~~rotate with the earth's surface, although their resolutions
77 are lower than that of polar-orbit satellites, they can capture the formation and
78 development of mesoscale convective systems by continuous monitoring (Montmerle
79 et al., 2007; Stengel et al., 2009; Zou et al., 2011).

80 Geostationary satellites are able to continuously detect a region at a higher

带格式的: 字体: 小四, 字体颜色: 文字 1

带格式的: 字体颜色: 文字 1

81 frequency, thus observing TCs over the vast ocean effectively. ~~In fact, they can~~
82 ~~capture convective spiral cloud systems relating to TCs.~~ As the first new generational
83 geostationary satellite, Himawari-8 plays a pioneering role for the geosynchronous
84 imagers to be launched in US, China, Korea and Europe. It has an advanced imager
85 called Advanced Himawari Imager (AHI) with 16 visible and infrared bands,
86 including 3 moisture channels, which can conduct a full-disk scan every 10 minutes.
87 Meanwhile, it can also acquire regional scanning images and that is to say it can scan
88 the Japan and the target areas every 2.5 minutes. Compared to the early
89 geosynchronous imagers, AHI has more spectrum bands and this can monitor the state
90 of atmosphere with a higher frequency.

91 In recent years, some experts and scholars have carried out some studies on the
92 data assimilation of geostationary satellite observations. Firstly utilizing [GSI](#)
93 ~~(~~[Gridpoint Statistical Interpolation \(GSI\)](#) from [National Centers for Environmental](#)
94 [Prediction NCEP \(NCEP National Centers for Environmental Prediction\)](#), Zou, et al
95 (2011) conducted direct assimilation on imagers' data from GOES-11 and GOES-12
96 to estimate their potential influences on [quantitative precipitation forecasts QPF](#)
97 ~~(QPF quantitative precipitation forecasts)~~ of coastal regions in the eastern part of
98 American. They found that assimilating radiance data from GOES's imager has a
99 remarkable improvement on 6 to 12 hour's QPF near northern Mexico Gulf coast.
100 Their work was continued by Qin, et al (2013), which put thinned radiance data into
101 GSI system to make a comprehensive investigation on the issue on combined

102 assimilation of GOES Imager data together with ~~AMSU-A Advance Microwave~~
103 ~~Sounding Unit-A (AMSU-A Advance Microwave Sounding Unit A)~~, ~~AMSU-B~~
104 ~~Advance Microwave Sounding Unit-B (AMSU-B Advance Microwave Sounding~~
105 ~~Unit B)~~, ~~Atmospheric Infrared Sounder AIRS (AIRS Atmospheric Infrared Sounder)~~,
106 ~~Microwave Humidity Sounder MHS (MHS Microwave Humidity Sounder)~~, ~~High~~
107 ~~Resolution Infrared Radiation Sounder HIRS (HIRS High Resolution Infrared~~
108 ~~Radiation Sounder)~~, ~~GOES Sounder GSN (GSN GOES Sounder)~~. The results showed
109 the effect of single assimilation of AHI radiance data are better than combined
110 assimilation in term of precipitation forecast. Zou, et al (2015) adopted the GSI
111 system to assimilate radiance data from four infrared channels on GOES-13/15 and
112 set up two experiments for comparison. A symmetric vortex was used for initialization
113 in the first experiment and an asymmetric counterpart for the other experiment.
114 Results showed that direct assimilation of GOES-13/15's radiance data could yield
115 positive effects on the track and intensity forecasts of hurricane "Debbie". As the new
116 instrument of himawari-8, there are few studies on the DA of himawari-8 data. Ma, et
117 al (2017) used ~~4D-EnVar~~ four-dimensional ensemble variational
118 ~~(4D-EnVar four-dimensional ensemble variational)~~ DA in NCEP's GSI system to
119 assimilate radiance of three moisture channels of AHI radiance data under clear-sky
120 condition and then NCEP GFS Global Forecast System (~~GFS Global Forecast System~~)
121 was utilized to estimate the impacts of AHI radiance data assimilation on ~~w~~ea~~t~~her
122 forecast. They found it had a positive impact on the forecast of global vapor at high
123 level of troposphere. Wang, et al (2018) investigated the impact of assimilating three

124 water vapor channels under clear sky on the analysis and forecast of a rainstorm in
125 Northern China with the 3DVAR method. It pointed out that the assimilation of AHI
126 radiance data could improve the wind and vapor fields and the accuracy of rainfall
127 forecast in the first 6 hours lead time.

128 Although previous researches have made several achievements in satellite data
129 assimilation and application, it is still a challenge to make more effective use of the
130 new generational geostationary satellite imager data with high spatial and temporal
131 resolution. In most of the previous studies, researches usually use a 6 hour's or even
132 longer time interval with a coarse spatial resolution. Therefore, the rapid updating
133 assimilation techniques of the geostationary satellite radiance data have not been well
134 carried out at convective scale. This study intends to build a data assimilation system
135 aiming at AHI radiance data based on the new generational mesoscale Weather
136 Research and Forecasting (WRF) model. A case of Typhoon Soudelor is studied by
137 performing numerical simulation to address the impacts of convective DA on the
138 improvement of the initial conditions of TC and the enhancement of track and
139 intensity forecasts. Our study focuses mainly on assimilating the three water vapor
140 channels (6.2, 6.9, and 7.3 μm) since they are very sensitive to the humidity in the
141 middle and upper troposphere and have a certain effect on the lower troposphere.
142 Thus, a large amount of effective atmospheric information can be provided for AHI
143 radiance data assimilation in the troposphere. The weighting functions for the three
144 channels are provided in Fig. 1.

145 Section 2 describes the observations and the data assimilation system. Introductions
146 to the typhoon case and the experimental setup are provided in section 3. The detailed
147 results in terms of the analyses and the forecasts are illustrated in section 4 before
148 conclusions are summarized in section 5.

149 **2. Observational data and DA system**

150 *2.1 An introduction to Himawari-8 AHI radiance data*

151 Himawari-8 satellite was launched by JMA to a geosynchronous orbit on 17
152 October 2014 and has begun its operational use since 7 July 2015 (Bessho et al.,
153 2016). It is located between the equator and 140.7°E, thus the earth is observed
154 between 60°N and 60°S meridionally and between 80°E and 160°W zonally.
155 Compared to its previous generation Himawari-7, its detective ability can get
156 significantly improved since the instrument AHI on Himawari-8. Besides, its device is
157 comparable to imagers on American GOES-R satellite (Goodman et al., 2012; Schmit
158 et al., 2005; Schmit et al., 2008; Schmit et al., 2017). AHI is able to provide a full-disk
159 image every 10 minutes and complete a scan over Japan every 2.5 minutes. AHI
160 conducts continuous scan and detection on a moving targeted typhoon. It has 16
161 channels covering visible, near-infrared, and infrared spectral bands with a resolution
162 of 0.5 km or 1 km, and 2 km respectively. Channel 8 to 10 (6.2, 6.9, and 7.3 μm) are
163 water vapor bands that are sensitive to the humidity in the middle and upper
164 troposphere (Di et al., 2016). Other channels (channel 11, 12, 16: 8.6 μm, 9.6 μm, and
165 13.3 μm) are either monitoring other fields such as the thin ice clouds, volcanic SO₂

166 gas, the ozone or CO₂, or the atmospheric window channels (13-15: 10.4, 11.2, and
167 12.4 μm) function as monitors for ice crystal/water, low water vapor, volcanic ash, sea
168 surface temperature and other phenomena (Bessho et al., 2016).

169 2.2 WRFDA system and AHI radiance data

170 WRFDA system is designed by National Center for Atmospheric Research
171 (NCAR) and it contains 3DVAR, 4DVAR, Hybrid parts. This research is based on the
172 3DVAR method. An interface that is suitable for AHI DA is built in WRFDA system.
173 Currently, WRFDA is able to assimilate many conventional and unconventional
174 observations. In terms of satellite radiance data, this system is compatible with [the](#)
175 [Radiative Transfer model of the Television and Infrared Observational Satellite](#)
176 [Operational Vertical sounder RTTOV](#) (~~RTTOV~~[the Radiative Transfer model of the](#)
177 [Television and Infrared Observational Satellite Operational Vertical sounder](#)) and
178 [Community Radiative Transfer Model](#) ~~CRTM~~ ([CRTM, Community Radiative Transfer](#)
179 [Model](#), Liu and Weng, 2006) as observation operators. In this study, CRTM is utilized
180 as the observation operator to simulate and compute AHI radiance data. Estimating
181 the systematic bias and random error of the observations caused by the errors of
182 numerical models and instruments are the key factors to directly assimilate the
183 satellite radiance data. Apart from eliminating cloud pixels, other procedures [are](#)
184 [implemented inside the data assimilation framework](#) for [the](#) quality control are as
185 follows. (1) when reading the data, remove the observed outliers with values below 50
186 K or above 550 K; (2) only the marine observations are applied by removing the

187 observations on the land and the observations over complex surfaces; (3) remove
 188 observations when the observation minus the background is larger than 3 times of the
 189 observation error; (4) the pixels are removed when the cloud liquid water path
 190 calculated by the background field of the numerical model is greater than or equal to
 191 0.2 kg/m²; (5) eliminate the data when the observation minus background is greater
 192 than 5 K. [These two parameters are used for these radiances on different sensors of](#)
 193 [various satellites such as AMSU-A, MHS, and the Advanced Microwave Scanning](#)
 194 [Radiometer 2 \(AMSR2\) \(Wang et al., 2018, Yang et al., 2016\).](#)

195 By using 3DVAR algorithm, the assumption is that there is no bias between
 196 observation and background (Dee et al., 2009; Liu et al., 2012; Zhu et al., 2014). A
 197 bias correction scheme for observation is essential before DA. Usually, radiance bias
 198 can be obtained by a linear combination of a set of forward operators.

$$199 \quad \tilde{H}(x, \beta) = H(x) + \beta_0 + \sum_{i=1}^{N_p} \beta_i p_i \quad (1)$$

200 Here, $H(x)$ represents the initial observation operator (before the bias
 201 correction), x represents the mode state vector, N_p is the number of the
 202 [predictions.](#) β_0 represents a constant component of the total bias (constant part),
 203 [while](#) p_i and β_i represent the i -th predictor and its coefficient respectively. In this
 204 study, four potentially state-dependent predictors (1000–300 hPa and 200–50 hPa
 205 layer thicknesses, surface skin temperature, and total column water vapor) are applied.
 206 The variational bias correction (VarBC) scheme is utilized to update the bias

域代码已更改

207 correction coefficient variationally with the new observation operator considered in
208 the cost function of 3DVAR.

209 **3. Introduction to the typhoon and experimental design**

210 *3.1 Typhoon Soudelor*

211 From the record of the China Meteorological Administration (CMA), Typhoon
212 Soudelor was the 13th typhoon in 2015 as the second strongest tropical cyclone in that
213 year. At 1200 UTC 30 July 2015, it formed at northwest Pacific Ocean as a tropical
214 storm at 13.6° N, 159.2° E, then moved north-westwards. It upgraded to a strong
215 tropical storm at 2100 UTC 1 August 2015. Afterwards, it went through a process of
216 rapid intensification. It became a typhoon at 0900 UTC 2 August 2015, a strong
217 typhoon at 2100 UTC 2 August 2015, a super typhoon at 0900 UTC 3 August 2015.
218 Then it weakened to a strong typhoon in the morning on 5 August 2015. However, it
219 intensified to a super typhoon again at 1200 UTC 7 August 2015 with a maximum
220 surface wind of 52 m s⁻¹, moving west by north, and its intensity raised to its second
221 peak. It was reduced to a strong typhoon again at 1800 UTC 7 August 2015. It
222 decreased to a typhoon, entering to Taiwan Strait. It landed again as a typhoon at 1410
223 UTC on the coast of Fujian Province, China. Owing to continuous orographic friction,
224 it decreased to a tropical depression. Fig. 2 shows the track of Soudelor and different
225 color lines represent typhoon's maximum surface wind. It is displayed that after the
226 formation of typhoon, its track is relatively stable. After July 30, the tropical
227 depression moved west by north at a speed of about 20 km/h. Its moving tendency

228 changed slightly within 10 days of its generation. However, its intensity went through
229 a rapid intensification, a weakening, a second intensification, ~~then following by~~ a
230 continuous weakening ~~till disappearing gradually~~ after landing on the China. Fig. 3
231 demonstrates the variation of typhoon's intensity from 31 July 2015 to 5 August 2015.
232 It is shown that typhoon's maximum surface wind increased fast, while its minimum
233 sea level pressure decreased sharply. This was the stage of typhoon's rapid
234 intensification. The ~~period~~~~date~~ from 1 August 2015 to 3 August 2015 during its rapid
235 intensification ~~are is~~ selected ~~as a research object~~.

236 3.2 Experimental design

237 Two experiments are designed to investigate the effects of AHI radiance data
238 direct assimilation on the analysis and forecast of Typhoon Soudelor starting from
239 1800 UTC 1 August 2015 to 0000 UTC 3 August 2015. WRF 3.9.1 is employed as the
240 forecast model in this experiment. Arakawa C grid is used in the horizon with a 5 km
241 grid distance. As is known, Arakawa A grid is "unstaggered" by evaluating all
242 quantities at the same point on each grid cell. The "staggered" Arakawa B-grid
243 separates the evaluation of the velocities at the grid center and masses at grid corners.
244 Arakawa C grid further separates evaluation of vector quantities compared to the
245 Arakawa B-grid. Vertically, it has 41 eta levels using 10 hPa as its top with coarser
246 vertical spacing for the higher levels. ~~The center of the model domain is located at~~
247 ~~(17.5 N, 140 E)~~~~Model center is (17.5 N, 140 E)~~ (Fig. 4). The initial condition and
248 lateral boundary are provided by 0.5°×0.5° Global Forecasting System (GFS)

带格式的: 字体: (中文) 黑体, 小四,
字体颜色: 文字 1

带格式的: 字体: (中文) 黑体

249 reanalysis data. The following parameterization schemes are used: The following
250 parameterization schemes are used: WDM6 microphysics scheme (Lim et al., 2010),
251 Grell Devenyi cumulus parameterization scheme (Grell et al., 2002), [Rapid Radiative](#)
252 [Transfer Model RRTM](#) (~~RRTM~~[Rapid Radiative Transfer Model](#)) longwave radiation
253 scheme (Mlawer et al., 1997), shortwave radiation scheme (Dudhia et al., 1989), and
254 YSU boundary layer scheme (Hong et al., 2006) .

255 The experimental procedures are illustrated by Fig. 5. Firstly, a 6-hour's spin-up
256 conducted initialized from 1800 UTC 1 August 2015 to prepare the background field
257 for the data assimilation at 0000 UTC 2 August 2015. [The 6-hour spin-up period is](#)
258 [commonly applied to initialize the typhoon or hurricane system the data assimilation](#)
259 [experiments, although longer spin-up period is also acceptable to introduce more](#)
260 [model errors in the background such as 12-hour or 24-hour.](#) The first experiment is
261 assimilating GTS (Global Telecommunications System) conventional data (including
262 aircraft report, ship report, sounding report, satellite cloud wind data, ground station
263 data) only, which is called control experiment (CTNL). Another experiment is
264 configured with AHI radiance data assimilation (AHI_DA). AHI radiance data is
265 assimilated hourly further from 0000 UTC to 0600 UTC on 2 August 2015.
266 Afterwards, a 48 hours forecast is launched as the deterministic forecast. The
267 climatological background error (BE) statistics are estimated using the National
268 Meteorological Center (NMC) method. There are 5 control variables applied in this
269 study including U component, V component, full temperature, full surface pressure,

270 and pseudo-relative humidity. The observation error for each channel is estimated
271 based on the observed brightness temperature minus background brightness
272 temperature (OMB) from 0000 UTC on 1 August 2015 to 0000 UTC on 3 August
273 2015 every 6 hours.

274 Fig. 4 also shows the distribution of GTS observation data at the simulated
275 domain at 0000 UTC 2 August 2015. It is proved that raw radiance observations
276 thinned to a grid with 2–6 times of the model grid resolution are able to remove the
277 potential error correlations between adjacent observations (Schwartz et
278 al., 2012; Xu et al., 2015; Choi et al., 2017). Hence, 20 km is chosen to make
279 thinning of AHI radiance data. Also, sensitivity experiments with 25 km, and 30 km
280 thinning mesh are also conducted with similar results (Wang et al., 2018). The length
281 scale and the variance scale are set to be 0.5 and 1 respectively after several
282 sensitivity experiments conducted on tuning the background error. Similar
283 conclusions are also found in Shen and Min (2015) with the scale factors related to
284 the static background error covariance.

285 4. Results

286 4.1 Minimization iterations

287 In this study, minimization stops when the norm of the gradient for the cost
288 function is reduced by a factor of 0.01, which is commonly used in data assimilation
289 procedures. Inner minimization stops either when the criterion of the cost function
290 gradient is met or when inner iterations reach 200. ~~minimization stops when the norm~~

带格式的: 字体: (中文) + 中文正文
(等线)

带格式的: 字体: (中文) 黑体, 小四,
字体颜色: 文字 1

带格式的: 字体: (中文) 黑体, 小四,
字体颜色: 文字 1

带格式的: 字体: (中文) 黑体, 小四,
字体颜色: 文字 1

带格式的: 字体颜色: 自动设置

带格式的: 字体: (中文) 黑体, 小四,
字体颜色: 自动设置

291 ~~of the gradient of the cost function gradient is reduced by a factor of 0.01, which is~~
292 ~~commonly used in data assimilation procedures. Inner minimization stops either when~~
293 ~~the criterion of the decrease of the cost function gradient is met or when inner~~
294 ~~iterations reach 200.~~ Fig. 6 shows the cost function and gradient with the iteration
295 times. It is found that, for this case, the criterion of the cost function gradient decrease
296 is met. There is an obvious exponential decrease curve in Fig. 6a, while Fig. 6b shows
297 gradient decreases with the increase of iteration times. It is seen from Taking Fig. 6a
298 as an example, that cost function decreases remarkably in the first 10 iterations.
299 However, after 30 times of iteration, the cost function curve becomes smooth
300 gradually. The differences between background field and observation ~~are were~~ largest.
301 With continuous iterations, background field goes through continued adjustments.
302 Finally, the cost function ~~tends tended~~ to reach a stable minimum that represents the
303 point when cost function has its optimal solution. Besides, the gradient in Fig. 6b
304 decreases stably generally with increasing iterations. The exponential decrease of the
305 cost function and the change trend of its gradient indicate that the effectiveness of
306 AHI radiance DA. The final iterated analytical field ~~is was~~ close to the observation.
307 The wall clock times used by CTNL and AHI DA for the data assimilation procedures
308 are rather comparable with roughly 30 minutes and 40 minutes on a Linux
309 workstation with 36 processors. It should be pointed out that computational cost of the
310 deterministic forecast and the pre-process for gribbed GFS data are same in these two
311 experiments.

312 4.2 Analytical results of the brightness temperature

313 Figs. 7a, c, and, e show the distribution of OMB, while the observed brightness
314 temperature minus ~~the analytical-simulated~~ brightness temperature from the analyses
315 (OMA) after the bias correction of AHI radiance data are presented in Figs. 7b, d, and
316 f from channels 8, 9, and 10 at 0000 UTC 2 August 2015. ~~It should be pointed that~~
317 even only parts of the AHI radiance data (roughly 20000 clear sky pixels of total
318 50000 pixels for each DA cycle) are applied after quality control in the data
319 assimilation, the radiative transfer model is able to simulate the brightness
320 temperature for all the model grid point with the background and the analysis
321 respectively for the verification purpose~~It should be pointed that even only parts of~~
322 ~~the AHI radiance data are applied after quality control in the data assimilation, the~~
323 ~~radiative transfer model is able to simulate the brightness temperature for all the~~
324 ~~pixels with the background and the analysis respectively for the verification purpose.~~

325 The similar verification method is also applied in Yang et al., (2016). In the Fig. 7a,
326 part of typhoon's spiral cloud belt ~~is-was~~ clearly visible. The brightness temperature in
327 typhoon's inner-core area ~~is-was~~ low, while the brightness temperature in other areas
328 ~~is-was~~ high. The mean of observed OMB was -4.65 K, indicating that the background
329 brightness temperature ~~is-was~~ higher than the observation. It is found in Fig. 7b that
330 the OMA values of most pixels ~~are-were~~ below 0.02 K, indicating that the analytical
331 field fitting the observation after analyzing. It can be inferred from Figs. 7a, c, and e
332 that the magnitude in OMB of channel 10 ~~is-was~~ generally larger than that of channel
333 9, while that of the OMB in channel 8 ~~is-was~~ the smallest. This is because the

带格式的: 字体: (中文) 黑体, 小四,
字体颜色: 文字 1

334 detection height of channel 10 ~~is was~~ lower than that of channel 8 and 9 seen from the
335 weighting function (Fig. 1), indicating channel 10 is largely affected by the clouds.
336 Conversely, the weighting peak of the channel 8 ~~is was~~ the highest, being least
337 affected by the clouds. In general, the ~~analytical simulated~~ brightness temperature
338 ~~from the analyses~~ matched well with the observed brightness temperature of all the
339 three water vapor channels after the assimilation of AHI radiance data.

340 ~~Fig. 8 shows~~To validate the effect of the bias correction for AHI radiance data at
341 0000 UTC 2 August 2015. ~~Fig. 8a, d, g show~~, the scatter plots of the observed
342 brightness temperature and the brightness temperature from the background before the
343 bias correction are shown in Figs. 8a, d, and g. Similarly, ~~Fig. 8b, e, h show~~the
344 results after the bias correction are provided in Figs. 8b, e, and h. Fig. 8c, f, i show the
345 ~~scatter plots of observed brightness temperature and analytical brightness temperature~~
346 ~~after bias correction~~. From Fig. 8a, before the bias correction, the values from the
347 observation and the background ~~are were~~ comparable, but most of the scatter points
348 ~~are were~~ below the diagonal line. This suggests that the observed brightness
349 temperature ~~is was~~ higher than the background simulated brightness temperature.
350 From Fig. 8b, after the bias correction, the observed warm bias ~~is was~~ corrected to
351 some extent. ~~From Fig. 8a, b, after the bias correction, with~~ the root mean square error
352 (RMSE) of OMB ~~decreases decreasing~~ from 1.864 K to 1.627 K, ~~with and~~ the average
353 decreasing from 0.956 K to 0.358 K, ~~proving the validity and rationality of the~~
354 ~~variational bias correction~~. The scatter plots of the observed brightness temperature
355 and the brightness temperature from the analyses after the bias correction are shown
356 in Figs. 8 c, f, and j. Compared to the result of Fig. 8b, the scatters in Fig. 8c ~~are were~~
357 more symmetrical, fitting closely to the diagonal line. The mean and RMSE were also
358 significantly reduced, suggesting that the analytical fields match better with the is
359 ~~more similar to~~ observation than background field. ~~Channel 9, 10 have a similar result,~~

带格式的: Default, 两端对齐, 段落间
距段后: 1.2 磅, 行距: 1.5 倍行距

360 ~~but with a significantly reduced mean and RMSE, indicating that the background field~~
361 ~~and analytical field of channel 9, 10 match better with the observation than channel 8~~
362 ~~does. Among them the RMSEs of channel 10 are smallest compared to those from~~
363 ~~channels 8 and 9 for the OMB and OMA samples, which is likely related to strict~~
364 ~~cloud detection scheme for channel 10 with rather lower detecting peak (Wang et~~
365 ~~al., 2018). Among them the RMSE of channel 10 is smallest as 0.234 K in Fig. 8;~~
366 ~~which is likely related to strict cloud detection scheme for channel 10 with rather~~
367 ~~lower detecting peak (Wang et al., 2018).~~

带格式的: 字体颜色: 文字 1

带格式的: 字体: (中文) 黑体, 字体颜色: 文字 1

带格式的: 字体: (中文) 黑体, 字体颜色: 文字 1

带格式的: 字体: (中文) 黑体, 字体颜色: 文字 1

带格式的: 字体: (中文) + 中文正文 (等线), 五号, 字体颜色: 蓝色

368 Fig. 9 shows the observation numbers, the mean, and the standard deviation of
369 OMB and OMA of channels 8, 9, and 10 before and after the bias correction. It can be
370 seen that after the quality control, 24057, 24181, 21785 observations are adopted in
371 the DA system for channels 8, 9, and 10, respectively. From the mean value of OMB
372 before the bias correction, the value of the three channels ~~is was~~ relatively small,
373 indicating that the simulated brightness temperature of the three channels ~~is was~~ close
374 to the observed brightness temperature. The lowest mean of 0.3 K ~~is was~~ found in
375 channel 10, indicating that the simulated brightness temperature of channel 10 ~~is was~~
376 closest to the observed brightness temperature. Bias correction effectively ~~corrects~~
377 ~~corrected~~ the systematic bias and reduces the mean value of observation residuals.
378 After the bias correction, the OMB mean value of the three channels significantly
379 decreases to nearly 0 K. With the bias correction, the simulated brightness
380 temperature ~~is was~~ almost the same as the observed brightness temperature. The
381 ~~analysis of the~~ standard deviation ~~(stdv)~~ of OMB ~~shows that the results are were~~
382 comparable before and after the bias correction, ~~since they are calculated by~~

带格式的: 字体颜色: 自动设置

带格式的: 字体: (中文) 黑体, 小四,
字体颜色: 自动设置

带格式的: 字体颜色: 自动设置

383 subtracting the mean of the bias. It is found that the bias was corrected effectively
384 with an overall same magnitude of bias for each pixel, leading the stdv almost same
385 before and after the bias correction. The standard deviation of OMA ~~decreases~~
386 ~~decreased~~ by about 80% compared to OMB, indicating that the analyses fit better with
387 the observations after the data assimilation. Differences between the standard
388 deviations of the OMB and OMA were statistically significant at the 95% level using
389 zero difference for the null hypothesis.

390 The RMSEs of the simulated brightness temperature by the NWP model before
391 and after the assimilation are also calculated against the AHI radiance observations.
392 Fig. 10 shows the RMSEs during the DA cycles for channels 8, 9, and 10. As can be
393 seen from Fig. 10, RMSE ~~decreases~~ ~~decreased~~ after each analysis in AHI_DA. The
394 most significant improvement ~~is~~ ~~was~~ from the first analysis cycle of channel 8, where
395 RMSE of the brightness temperature after assimilation significantly decreases from
396 1.64 K to 0.46 K, possibly due to the largest adjustment on the background for the
397 first analysis time. The background before the assimilation ~~is~~ ~~was~~ the short-term
398 forecast from the previous analysis. The increase of the RMSE in the fluctuation
399 ~~arised~~ from the model error in the 1 hour short-term forecast. Overall, the effect of the
400 analysis from the channel 10 ~~is~~ ~~was~~ most significant.

401 *4.3 Analysis of the typhoon structure*

402 Fig. 11 shows the wind field at sea level and the distribution of water vapor at
403 850 hPa at 0000 UTC 2 August 2015. The obvious cyclonic eddy circulation

404 structures in the core area of the typhoon are found in both fields, while the
405 anti-cyclonic circulation ~~exists~~existed in the northwest quadrant of the typhoon. The
406 mixing ratio of water vapor in the region where the typhoon located ~~is~~was very high
407 and the wind field is cyclonic, indicating that the typhoon has a continuous water
408 vapor advection. This ~~contributes~~contributed to the enhancement of typhoon
409 (Kamineni, et al., 2003). From the flow field of the control experiment in Fig. 11a, the
410 water vapor convergence in the center of the typhoon region ~~is~~was weak with the low
411 intensity and smaller coverage. As can be seen from Fig. 11b, after the assimilation of
412 AHI radiance data, the streamlines in the typhoon region become denser, indicating
413 that the cyclonic circulation ~~is~~was strengthened. Conversely, the intensity and
414 distribution of the water vapor after the assimilation of AHI radiance data tend to
415 contribute to the developing typhoon. This suggests that the field outside of the
416 typhoon center was also adjusted as the assimilation of AHI radiance data ~~are~~
417 were able to ~~significantly~~ improve the large-scale environmental field in the
418 simulation region of Typhoon Soudelor. It should be pointed out that the model status
419 in the cloudy area ~~are~~were modified due to the spatial correlation in the background
420 error covariance. The similar findings for small-scale information in the cloudy area
421 can also be referred in Wang et al., (2018).

422 4.4 Track forecast

423 In order to further evaluate the effect of AHI radiance data assimilation, a 48-hour
424 deterministic forecast ~~is~~was launched with the analyses initialized from 0000 UTC 2

带格式的: 字体: (中文) 黑体, 小四,
字体颜色: 文字 1

带格式的: 字体: (中文) 黑体, 小四,
字体颜色: 文字 1

带格式的: 字体: (中文) 黑体, 图案:
清除

425 August 2015 and 0600 UTC 2 August 2015 respectively. The best track data are
426 provided by the CMA (Yu et al., 2007; Song et al., 2010). The improvement is most
427 obvious at the start and end point. As can be seen in Fig. 12a, at the beginning of the
428 forecast, the initial location of the typhoon from the CTNL experiment has large south
429 bias and east bias at 0000 UTC and 0600 UTC respectively. Conversely, the location
430 of the typhoon in AHI_DA is relatively closer to the observation at the beginning. As
431 can be seen in Fig. 12a, at the beginning of the forecast, the initial location of the
432 typhoon from the CTNL experiment has large south bias and east bias at 0000 UTC
433 and 0600 UTC respectively. Conversely, the location of the typhoon in AHI_DA is
434 relatively closer to the observation at the beginning. During the following few hours
435 of forecasts, the typhoon track predicted by the CTNL continues to show a south-west
436 bias with the environmental wind, while the track predicted by AHI_DA match better
437 with the best track. Fig. 12c shows the averaged typhoon track error over the two
438 forecasts predicted by the two experiments. At the initial time of the forecast, the track
439 errors of CTNL and AHI_DA ~~are~~ were significantly different, with the magnitude of
440 55.6 km and 13.4 km, respectively. During the subsequent 48-hour forecast, the track
441 error of the CTNL gradually increases with the forecast time reaching 167.1 km at the
442 end of the forecast. In contrast, the track error of AHI_DA is consistently less than
443 122.5 km during the 48-hour forecast period. In general, the average track error of the
444 CTNL is 168.57 km, and the average track error of AHI_DA experiment is only 67.0
445 km, indicating a significant improvement in the track prediction.

带格式的: 字体: (中文) 黑体

带格式的: 字体: (中文) 黑体, 小四,
字体颜色: 文字 1

带格式的: 字体颜色: 文字 1

带格式的: 字体颜色: 文字 1

446 Fig. 13 provides the time series of the typhoon intensity from the two
447 experiments in terms of the averaged maximum surface wind and minimum sea level
448 pressure error over the two forecasts initialized from 0000 UTC 2 August 2015 and
449 0600 UTC 2 August 2015 respectively. It can be seen that the maximum surface wind
450 error predicted by the AHI_DA ~~is was~~ much lower than that by the CTNL for the first
451 30 hours, due to the overall under estimation for the ~~strength-intensity~~ of Typhoon
452 Soudelor simulated in the background field. The maximum surface wind errors of
453 AHI DA are generally smaller than those of CTNL. It should be pointed out that the
454 difference between the maximum surface wind errors of the two experiments reaches
455 up to 7.5 m s-1 after 24-hour forecast.~~The maximum surface wind predicted by~~
456 ~~AHI DA fit closer to the best track data with the maximum difference about 2.63.5 m~~
457 ~~s-1 after 12 hours forecast.~~ In Fig. 13b, the results of the minimum sea level pressure
458 are consistent with Fig. 13a, while the improvement for the minimum sea level
459 pressure exists lasts for 40 hours.

带格式的: 字体: (中文) 黑体, 小四, 字体颜色: 文字 1

带格式的: 字体: (中文) 黑体, 字体颜色: 文字 1

带格式的: 字体颜色: 文字 1

带格式的: 字体: (中文) 黑体

带格式的: 字体: (中文) 黑体

460 5. Conclusion

461 An interface for AHI radiance data assimilation on the WRFDA system based on
462 the 3DVAR assimilation method was built. Based on the Typhoon Soudelor in 2015,
463 ~~two~~ two experiments for comparison was designed to examine the impact of AHI
464 water vapor channel radiance data assimilation on the analysis and prediction of the
465 rapid development stage of Typhoon Soudelor under clear sky condition. Following
466 conclusions are obtained:

467 (1) The AHI radiance data on the new generation of geostationary meteorological
468 satellite is able to reflect the structure of Typhoon Soudelor very clearly. After a series
469 of pre-procedures such as the quality control, the bias correction, cloudy pixels are
470 able to effectively be eliminated, ensuring the validity and rationality of the Ahi
471 radiance data. The biases are also eliminated from the VarBC statistical method,
472 which is able to provide a positive impact on the data assimilation procedure for the
473 typhoon numerical simulation.

474 (2) Compared with the control experiment with only GTS data, the 3DVAR
475 assimilation including AHI radiance data is able to improve the structure of typhoon's
476 core and outer rain band. Also, the position and intensity of typhoon in the
477 background field are able to be corrected.

478 (3) ~~It is found that~~Generally, the track, ~~maximum surface wind, and and~~ minimum sea
479 level pressure from the AHI radiance data assimilation experiment match better with
480 the best track than the control experiment does for the subsequent ~~1848~~-hour forecast.
481 The maximum surface wind forecast error is reduced only for the first 30-hour.

482 In this study, the AHI water radiance data assimilation is conducted under the
483 clear sky condition. The results of the experiments indicate that AHI radiance data
484 assimilation has a positive effect on the analysis and prediction of rapidly intensifying
485 TC. Although, the whole developing stages of Typhoon Soudelor include a rapid
486 intensification, a weakening, a second intensification, only the first intensification
487 during 1 August to 4 August considered as the numerical period. It is worth

带格式的: 字体颜色: 文字 1

带格式的: 字体: (中文) 黑体, 字体颜色: 文字 1, 图案: 清除

带格式的: 字体颜色: 文字 1

带格式的: 字体: (中文) 黑体, 小四, 字体颜色: 文字 1

带格式的: 字体颜色: 文字 1

488 [investigating the impact of AHI data assimilation on the whole period including the](#)
489 [first intensification, a weakening, and the second intensification of Typhoon Soudelor](#)
490 [to fully prove the advantages of AHI radiance data assimilation.](#) Considering the
491 complex influence of underlying surface, only the rapid development stage of typhoon
492 at sea were studied, while the whole generation, development and disappearance stage
493 of typhoon can also be studied in the future. In addition, based on the AHI radiance
494 data of the water vapor channels under the condition of clear sky, only 3DVAR
495 method was adopted. Further improvements under the condition of all sky and hybrid
496 DA can be obtained in the future.

497 **Acknowledgments**

498 This research was primarily supported by the Chinese National Natural Science
499 Foundation of China (G41805016), the Natural Science Foundation of Jiangsu
500 Province (BK20170940), the Chinese National Natural Science Foundation of China
501 (G41805070), the Chinese National Key R&D Program of China (2018YFC1506404,
502 2018YFC1506603), the research project of Heavy Rain and Drought-Flood Disasters
503 in Plateau and Basin Key Laboratory of Sichuan Province in China (SZKT201901,
504 SZKT201904), the research project of the Institute of Atmospheric Environment,
505 China Meteorological Administration, Shenyang in China (2020SYIAE07,
506 2020SYIAE02).

507

带格式的: 字体: (中文) 黑体, 小四,
字体颜色: 文字 1

带格式的: 字体颜色: 文字 1

508

References

509 Bauer, P., Geer, A.J., Lopez, P., and Salmond, D.: Direct 4D-Var assimilation of
510 all-sky radiance. Part I: Implementation, Quarterly Journal of the Royal
511 Meteorological Society, 136, 1868-1885, 2010.

512 Bauer, P., Auligné, T., Bell, W., Geer, A., Guidard, V., Heilliette, S., et al: Satellite
513 cloud and precipitation assimilation at operational NWP centres, Quarterly Journal of
514 the Royal Meteorological Society, 137, 1934-1951, 2011.

515 Bessho, K., Date, K., Hayashi, M., Ikeda, A., Imai, T., Inoue, H., et al.: An
516 introduction to Himawari-8/9—Japan's new-generation geostationary meteorological
517 satellites, Journal of the Meteorological Society of Japan, 94, 151-183, 2016.

518 Buehner, M., Caya, A., Carrieres, T., and Pogson, L.: Assimilation of SSMIS and
519 ASCAT data and the replacement of highly uncertain estimates in the Environment
520 Canada Regional Ice Prediction System, Quarterly Journal of the Royal
521 Meteorological Society, 142, 562-573, 2016. Choi, Y., Cha, D.-H., Lee, M.-I., Kim,
522 J., Jin, C.-S., Park, S.-H., and Joh, M.-S.: Satellite radiance data assimilation for
523 binary tropical cyclone cases over the western North Pacific, J. Adv. Model. Earth
524 Syst., 9, 832-853, 2017.

525 Dee, D.P., and Uppala, S.: Variational bias correction of satellite radiance data in the
526 ERA-Interim reanalysis, Quarterly Journal of the Royal Meteorological Society, 135,
527 1830-1841, 2009.

528 DeMaria, M., Sampson C.R., Knaff J.A., and Musgrave K.D.: Is tropical cyclone
529 intensity guidance improving? Bulletin of the American Meteorological Society, 95,
530 387-398, 2014.

531 Derber, J.C., and Wu, W.S.: The use of TOVS cloud-cleared radiance in the NCEP
532 SSI analysis system, Mon. Wea. Rev, 126, 2287-2299, 1998.

533 Di, D., Ai, Y., Li, J., Shi, W., and Lu, N.: Geostationary satellite-based 6.7 μm band
534 best water vapor information layer analysis over the Tibetan Plateau, Journal of
535 Geophysical Research: Atmospheres, 121, 4600-4613, 2016.

536 Dudhia, J.: Numerical Study of Convection Observed during the Winter Monsoon
537 Experiment Using a Mesoscale Two-Dimensional Model, Journal of the Atmospheric
538 Sciences, 46, 3077-3107, 1989.

539 [Geer, A. J., Baordo, F., Bormann, N., English, S., Kazumori, M., Lawrence, H., Lean,
540 P., Lonitz, K., and Lupu, C.: The growing impact of satellite observations sensitive to
541 humidity, cloud and precipitation, Quart. J. Roy. Meteorol. Soc., 143, 3189-3206.](#)

542 Goodman, S.J., Gurka, J., DeMaria, M., Schmit, T.J., Mostek, A., Jedlovec, G., et al.:
543 The GOES-R proving ground: Accelerating user readiness for the next-generation
544 geostationary environmental satellite system, Bulletin of the American Meteorological
545 Society, 93, 1029-1040, 2012.

546 Grell G.A., Dévényi D.: A generalized approach to parameterizing convection
547 combining ensemble and data assimilation techniques, Geophys. Res. Let., 29,
548 587-590, 2002.

带格式的: 字体: (中文) 等线, 小四, 字体颜色: 黑色

带格式的: 定义网格后不调整右缩进, 段落间距段后: 0 磅, 行距: 1.5 倍行距, 不调整西文与中文之间的空格, 不调整中文和数字之间的空格

带格式的: 字体: (中文) 等线, 小四, 字体颜色: 黑色

549 Hilton, F., Atkinson, N. C., English, S. J., and Eyre, J. R.: Assimilation of IASI at the
550 Met Office and assessment of its impact through observing system experiments,
551 Quarterly Journal of the Royal Meteorological Society, 135, 495-505, 2009.

552 Hong S.Y., Noh Y., Dudhia J.: A New Vertical Diffusion Package with an Explicit
553 Treatment of Entrainment Processes. Mon. Wea. Rev, 134, 2318-2341, 2006.

554 Jung, J.A., Zapotocny, T.H., Le Marshall, J.F., and Treadon, R.E.: A two-season
555 impact study on NOAA polar-orbiting satellites in the NCEP Global Data
556 Assimilation System, Weather Forecasting, 23, 854-877, 2008.

557 Kamineni, R., Krishnamurti, T., Ferrare, R., Ismail, S., and Browell, E.: Impact of
558 high resolution water vapor cross-sectional data on hurricane forecasting, Geophysical
559 Research Letters, 30, 38-1, 2003. Kazumori, M.: Satellite radiance assimilation in the
560 JMA operational mesoscale 4DVAR system, Mon. Wea. Rev, 142, 1361-1381, 2014.

561 Li, X., and Zou, X.: Bias characterization of CrIS radiances at 399 selected channels
562 with respect to NWP model simulations, Atmospheric Research, 196, 164-181, 2017.

563 Lim, K.-S. S., and Hong, S.-Y.: Development of an effective double-moment cloud
564 microphysics scheme with prognostic cloud condensation nuclei (CCN) for weather
565 and climate models. Mon. Wea. Rev, 138, 1587-1612, 2010.

566 Liu, Z., Schwartz, C.S., Snyder, C., and Ha, S.Y.: Impact of assimilating AMSU-A
567 radiance on forecasts of 2008 Atlantic tropical cyclones initialized with a limited-area
568 ensemble Kalman filter, Mon. Wea. Rev., 140, 4017-4034, 2012.

569 Liu, Q., and Weng, F.: Advanced doubling-adding method for radiative transfer in
570 planetary atmosphere. *J. Atmos. Sci.*, 63, 3459–3465, 2006.

571 Ma, Z., Maddy E.S., Zhang B., Zhu T., and Boukabara S.A.: Impact Assessment of
572 Himawari-8 AHI Data Assimilation in NCEP GDAS/GFS with GSI, *J. Atmos.*
573 *Oceanic Technol.*, 34, 797-815, 2017.

574 McNally, A.P., Watts, P.D., Smith, J.A., Engelen, R., Kelly, G.A., Thépaut, J.N.,
575 and Matricardi, M.: The assimilation of AIRS radiance data at ECMWF, *Quarterly*
576 *Journal of the Royal Meteorological Society*, 132, 935-957, 2006.

577 Minamide, M., and Zhang F.: Assimilation of all-sky infrared radiances from
578 himawari-8 and impacts of moisture and hydrometer initialization on
579 convection-permitting tropical cyclone prediction. *Mon. Wea. Rev.*, 146, 3241-3258,
580 2018.

581 Mlawer E.J., Taubman S.J., Brown P.D., et al.: Radiative transfer for inhomogeneous
582 atmospheres: RRTM, a validated correlated-k model for the longwave, *Journal of*
583 *Geophysical Research Atmospheres*, 102, 16663-16682, 1997.

584 Montmerle, T., Rabier, F., and Fischer, C.: Relative impact of polar-orbiting and
585 geostationary satellite radiance in the Aladin/France numerical weather prediction
586 system, *Quarterly Journal of the Royal Meteorological Society*, 133, 655-671, 2007.

587 Noh Y., Cheon W.G., Hong S.Y., et al.: Improvement of the K-profile Model for the
588 Planetary Boundary Layer based on Large Eddy Simulation Data, *Boundary-Layer*

589 Meteorology, 107, 401-427, 2003.

590 Prunet, P., Thépaut, J.N., Cassé V., Pailleux, J., Baverez, A., and Cardinali,
591 C.: Strategies for the assimilation of new satellite measurements at Météo-
592 France, *Advances in Space Research*, 25, 1073-1076, 2000.

593 Qin, Z., Zou, X., Weng, F.: Evaluating Added Benefits of Assimilating GOES Imager
594 Radiance Data in GSI for Coastal QPFs, *Mon. Wea. Rev.*, 141, 75-92, 2013.

595 Rennie, M.P.: The impact of GPS radio occultation assimilation at the Met
596 Office, *Quarterly Journal of the Royal Meteorological Society*, 136, 116-131, 2010.

597 Schmit, T.J., Gunshor, M.M., Paul Menzel, W., Gurka, J., Li, J., and Bachmeier,
598 S.: Introducing the next-generation advanced baseline imager (ABI) on
599 GOES-R, *Bulletin of the American Meteorological Society*, 86, 1079-1096, 2005.

600 Schmit, T.J., Li, J., Li, J., Feltz, W.F., Gurka, J.J., Goldberg, M.D., and Schrab,
601 K.J.: The GOES-R Advanced Baseline Imager and the continuation of current sounder
602 products, *Journal of Applied Meteorology and Climatology*, 47, 2696-2711, 2008.

603 Schmit, T.J., Griffith, P., Gunshor, M.M., Daniels, J.M., Goodman, S.J., and Lehair,
604 W.J.: A closer look at the ABI on the GOES-R series, *Bulletin of the American
605 Meteorological Society*, 98, 681-698, 2017.

606 | Schwartz, C. S., Liu, Z., Chen, Y. and Huang X.-Y.: Impact of assimilating
607 microwave radiances with a limited - area ensemble data assimilation system on
608 forecasts of Typhoon Morakot, *Weather Forecasting*, 27, 424-437, 2012.

609 Shen, F., and Min, J.: Assimilating AMSU-A radiance data with the WRF hybrid
610 En3DVAR system for track predictions of Typhoon Megi (2010), Advances in
611 Atmospheric Sciences, 32, 1231-1243, 2015.

612 Song J-J, Wang Y, Wu L.: Trend discrepancies among three best track data sets of
613 western North Pacific tropical cyclones. J. Geophys. Res. 115: D12128, DOI:
614 10.1029/2009JD013058, 2010.

615 Stengel, M., Undén, P., Lindskog, M., Dahlgren, P., Gustafsson, N., and Bennartz, R.:
616 Assimilation of SEVIRI infrared radiance with HIRLAM 4D-Var, Quarterly Journal
617 of the Royal Meteorological Society, 135, 2100-2109, 2009.

618 Wang, Y., Liu, Z., Yang, S., Min, J., Chen, L., Chen, Y., and Zhang, T.: Added value of
619 assimilating Himawari-8 AHI water vapor radiances on analyses and forecasts for
620 “7.19” severe storm over north China, Journal of Geophysical Research: Atmospheres,
621 123, 3374-3394, 2018.

622 Xu, D., Liu, Z., Huang, X.-Y., Min, J., and Wang, H.: Impact of assimilation IASI
623 radiances on forecasts of two tropical cyclones, Meteorology and Atmospheric
624 Physics, 122, 1-18, 2013.

625 | Xu, D., Huang, X.-Y., Wang H., Mizzi, A. P. and Min J.: Impact of assimilating
626 radiances with the WRFDA ETKF/3DVAR hybrid system on prediction of two
627 typhoons in 2012, J. Meteorol. Res, 29, 28-40, 2015.

628 | [Yan, B., Weng, F., and Derber, J., Assimilation of satellite microwave water vapor](#)

带格式的: 字体: (中文) 等线, 小四,
字体颜色: 黑色

带格式的: 定义网格后不调整右
缩进, 段落间距段后: 0 磅, 行距: 1.5
倍行距, 不调整西文与中文之间的
空格, 不调整中文和数字之间的空格

带格式的: 字体: (中文) 等线, 小四,
字体颜色: 黑色

带格式的: 字体: (中文) 等线, 小四,
字体颜色: 黑色

629 | [sounding channel data in NCEP Global Forecast System \(GFS\), paper presented at](#)
630 | [17th International TOVS Study Conference, Int. ATOVS Working Group, Monterrey,](#)
631 | [Calif, 2010.](#)

632 | Yang, C., Liu, Z., Bresch, J., Rizvi, S. R. H, Huang, X.-Y., and Min, J.: AMSR2
633 | all-sky radiance assimilation and its impact on the analysis and forecast of Hurricane
634 | Sandy with a limited-area data assimilation system, *Tellus A: Dynamic Meteorology*
635 | and *Oceanography*, 68, 2016.

636 | Yu H, Hu C, Jiang L.: Comparison of three tropical cyclone intensity datasets. *Acta*
637 | *Meteorol. Sin.* 21, 121-128, 2007.

638 | Zapotocny, T.H., Jung, J.A., Le Marshall, J.F., and Treadon, R.E.: A two-season
639 | impact study of satellite and in situ data in the NCEP Global Data Assimilation
640 | System, *Weather Forecasting*, 22, 887-909, 2007.

641 | Zhu, Y., Derber, J., Collard, A., Dee, D., Treadon, R., Gayno, G., and Jung,
642 | J.A.: Enhanced radiance bias correction in the National Centers for Environmental
643 | Prediction's Gridpoint Statistical Interpolation data assimilation system, *Quarterly*
644 | *Journal of the Royal Meteorological Societ*, 140, 1479-1492, 2014.

645 | Zou, X., Qin, Z., and Weng, F.: Improved coastal precipitation forecasts with direct
646 | assimilation of GOES-11/12 imager radiance, *Mon. Wea. Rev.* 139, 3711-3729, 2011.

647 | Zou, X., Qin Z., and Zheng Y.: Improved tropical storm forecasts
648 | with GOES-13/15 imager radiance assimilation and asymmetric vortex initialization
649 | in HWRF, *Mon. Wea. Rev.* 143, 2485-2505, 2015.

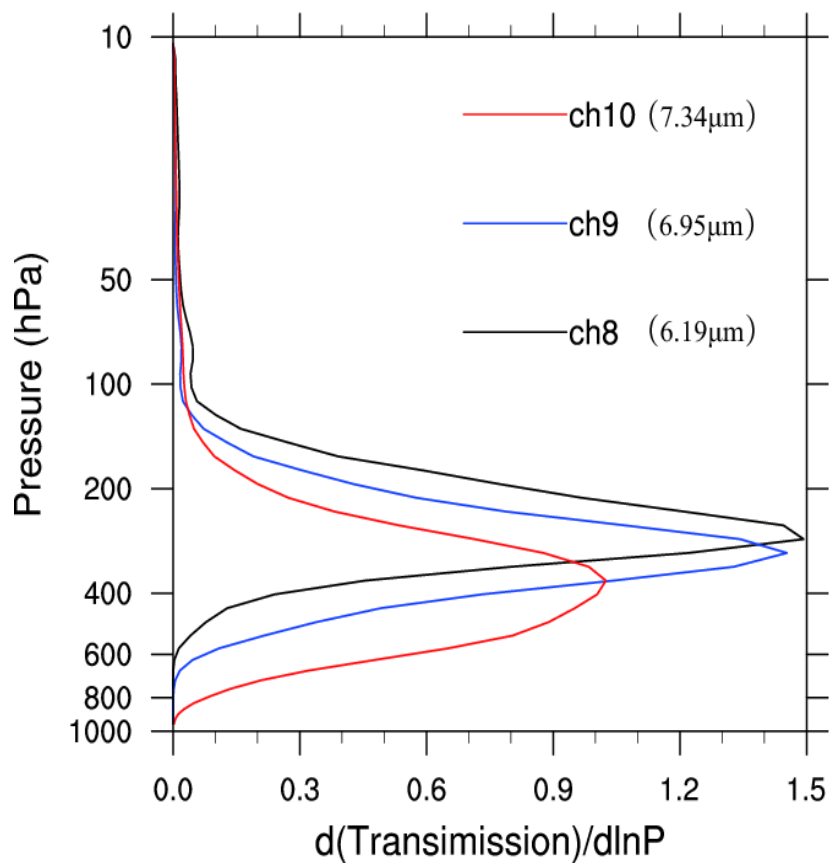
650

651

652

List of Figures

653



654

655 Fig.1 Weighting functions of Himawari-8 Advanced Himawari Imager three water

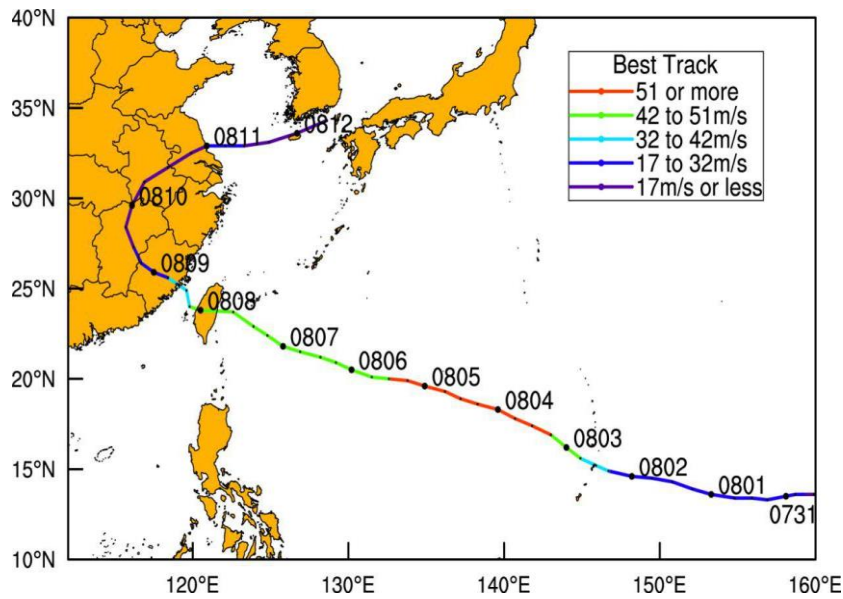
656 vapor channels for Channel 8, 9, and 10.

657

658

659

660



661

662 Fig.2 The best track of Soudelor from the China Meteorological Administration
663 (CMA) from 0000 UTC 30 July to 0600 UTC 12 August 2015. Different colors
664 represent intensity changes.

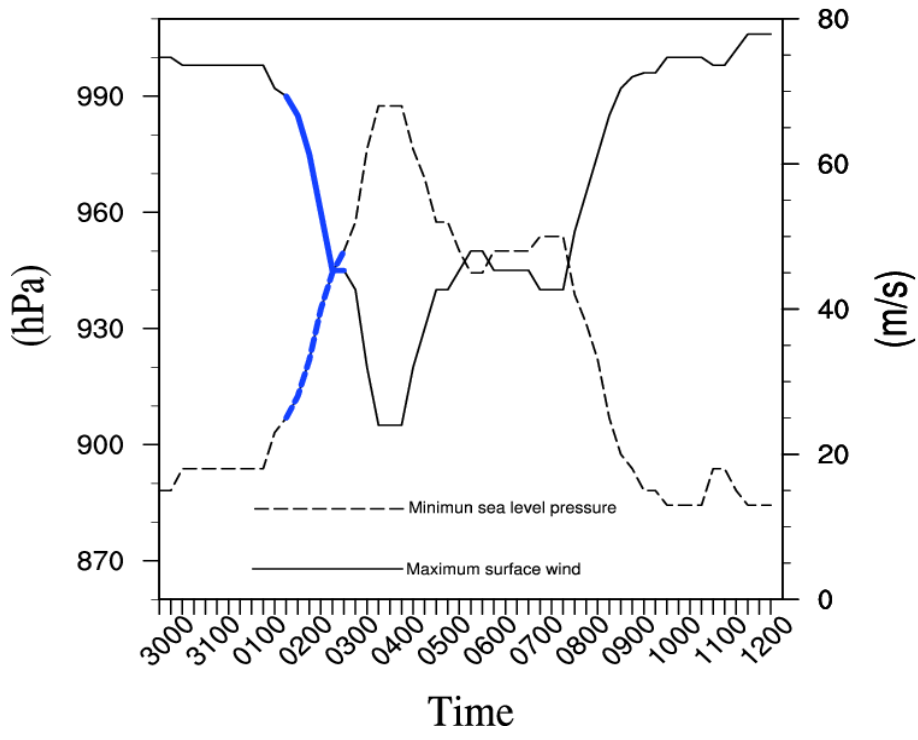
665

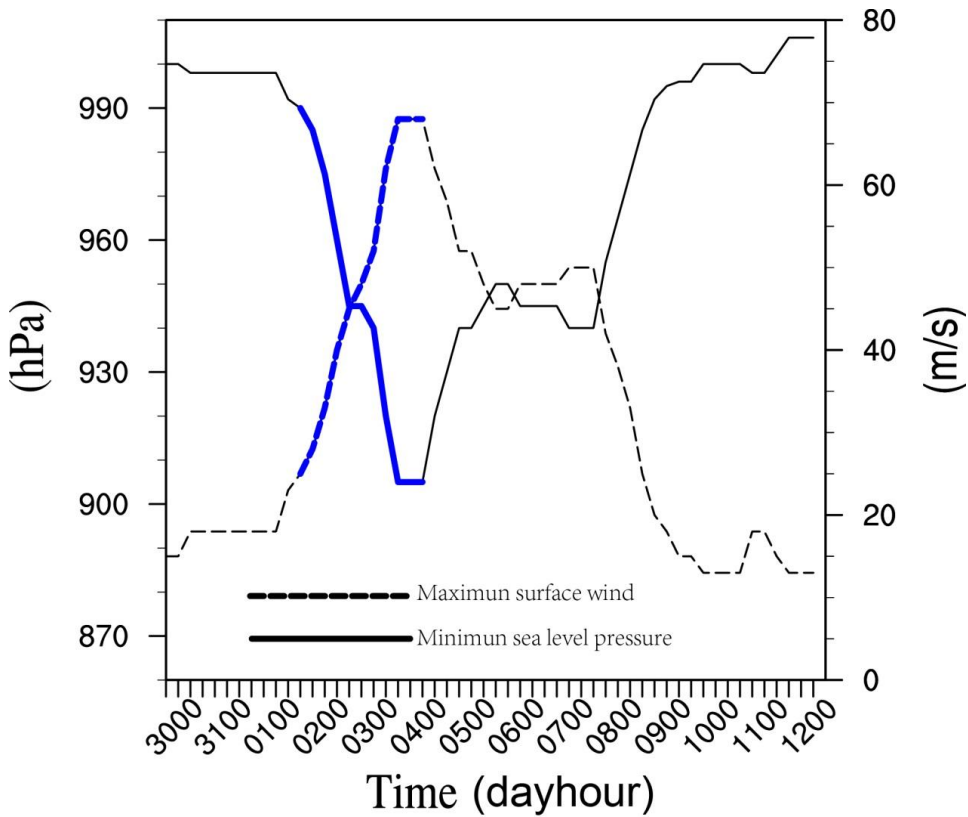
666

667

668

669





672

673 Fig. 3 The time series of the minimum sea level pressure (solid line, unit: hPa) and the
 674 maximum surface wind (dash line, unit: $m s^{-1}$) of ~~typhoon~~-Typhoon Soudelor from the
 675 CMA best-track data. from 0000 UTC 30 July 2015 to 0600 UTC 12 August 2015.

676 The specific period for the numerical results from 1800 UTC 1 August 2015 to 00600

677 UTC 34, August 2015 is highlighted in blue.

678

679

680

681

带格式的: 上标

带格式的: 字体: (中文) 宋体, 字体颜色: 文字 1

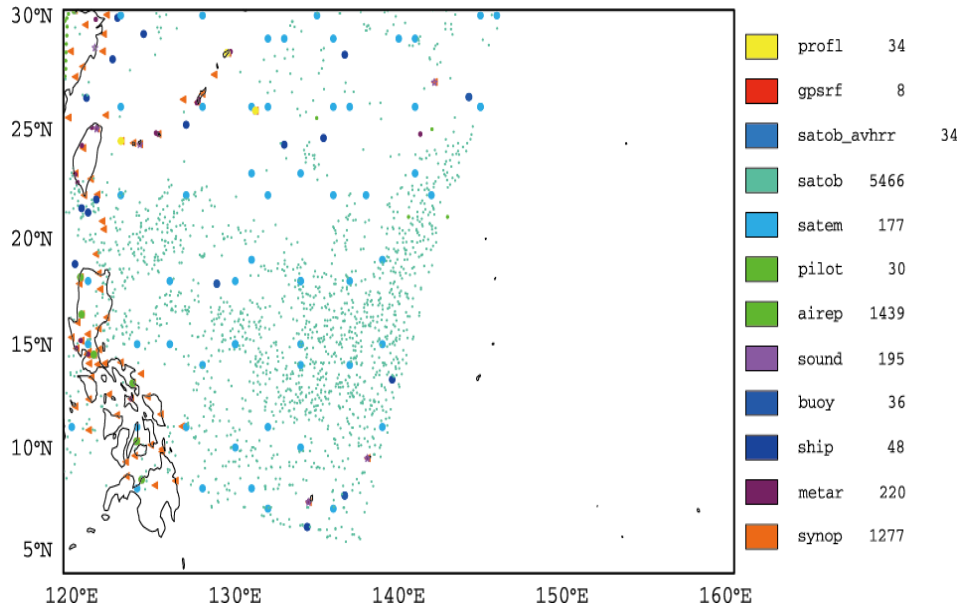
带格式的: 字体: (中文) 宋体, 字体颜色: 文字 1

带格式的: 字体: (中文) 宋体, 字体颜色: 文字 1

带格式的: 字体: (中文) 宋体, 字体颜色: 文字 1

682

683



684

685 Fig. 4 Distribution of GTS observations in the simulated area at 0000 UTC 2 August
686 2015. On the right side of the map is the name of observation data and the number of
687 observations. Each observation type is marked with different color along with a
688 unique symbol.

689

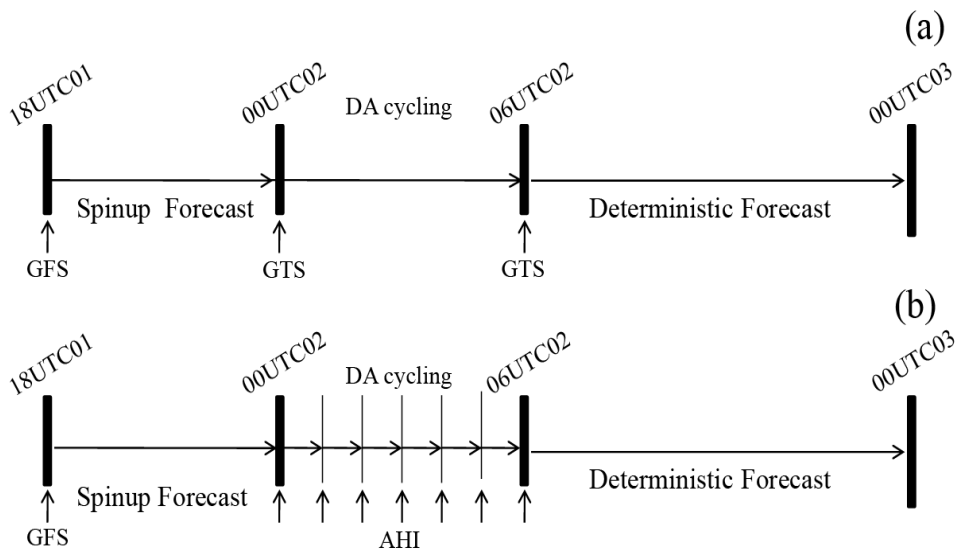
690

691

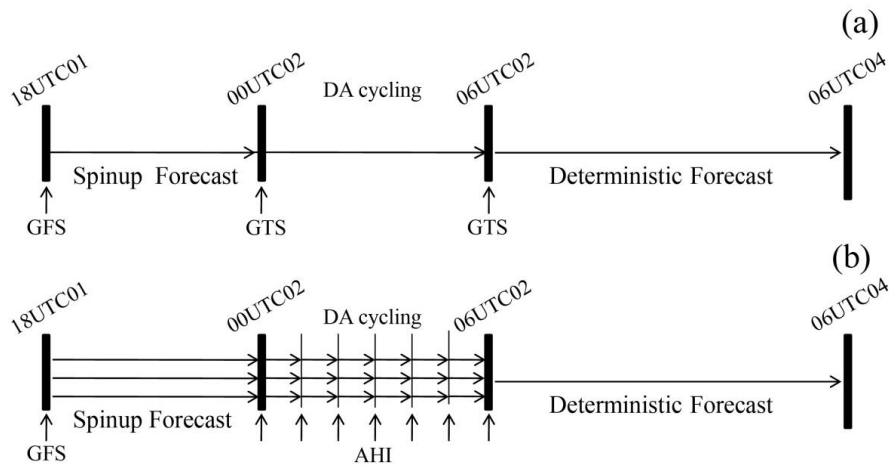
692

693

694



695



696

697 Fig. 5 The flow chart of the data assimilation experiments. (a) CTNL, (b) AHI_DA

698

699

700

701

702

703

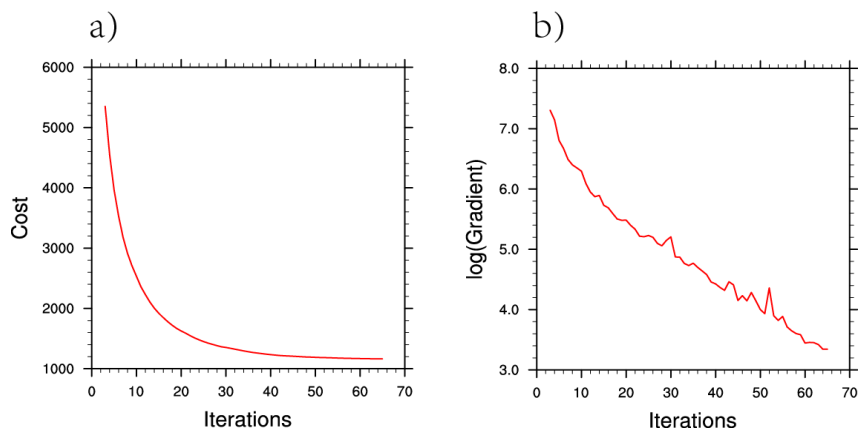
704

705

706

707

708



709

710 Fig. 6 (a) Cost function as functions of iterations, (b) gradient as functions of
711 iterations.

712

713

714

715

716

717

718

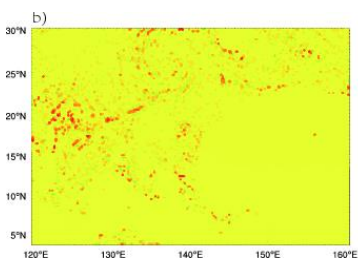
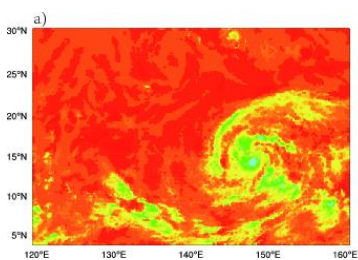
719

720

721

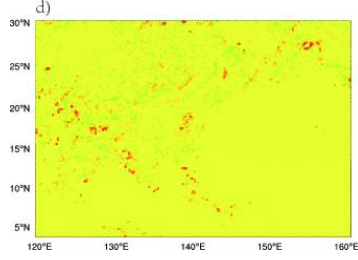
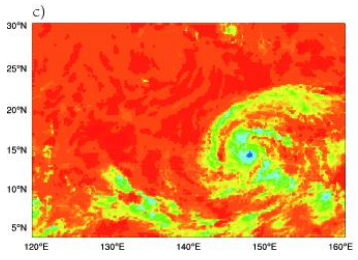
ch8(6.19 μ m)

722

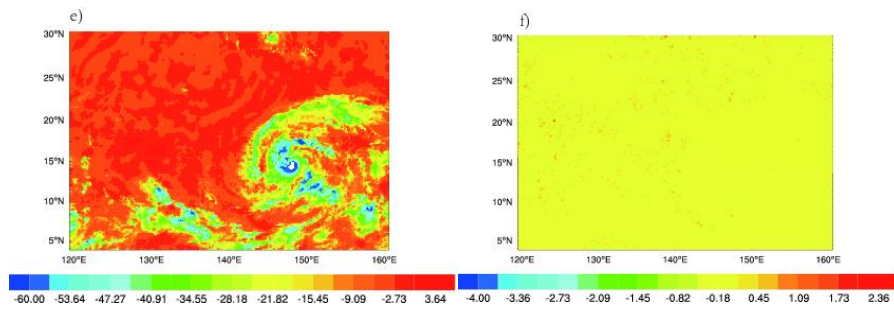


ch9(6.95 μ m)

723



ch10 (7.34 μm)



724

725 Fig. 7 (a, c, and e) OMB (unit: K) after bias correction for channel 8, 9, and 10,
726 respectively; (b, d, and f) OMA (unit: K) after bias correction for channel 8, 9, and 10,
727 respectively at 0000 UTC 2 August 2015.

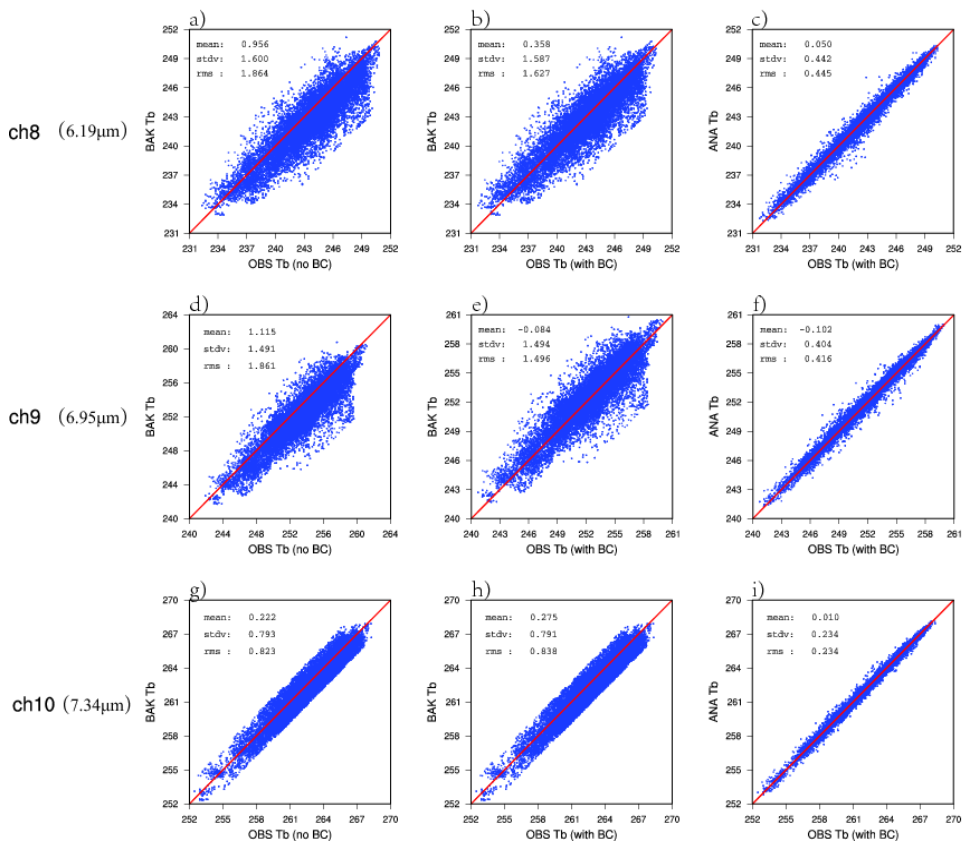
728

729

730

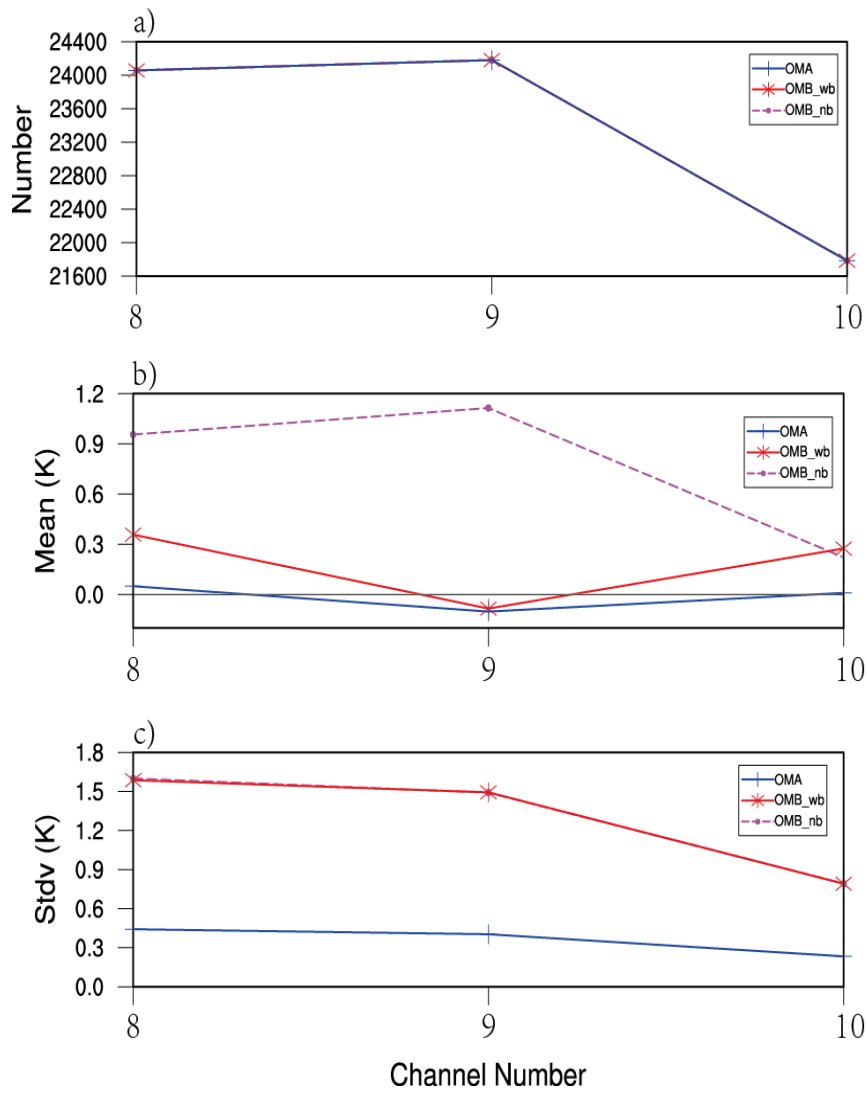
731

732



733

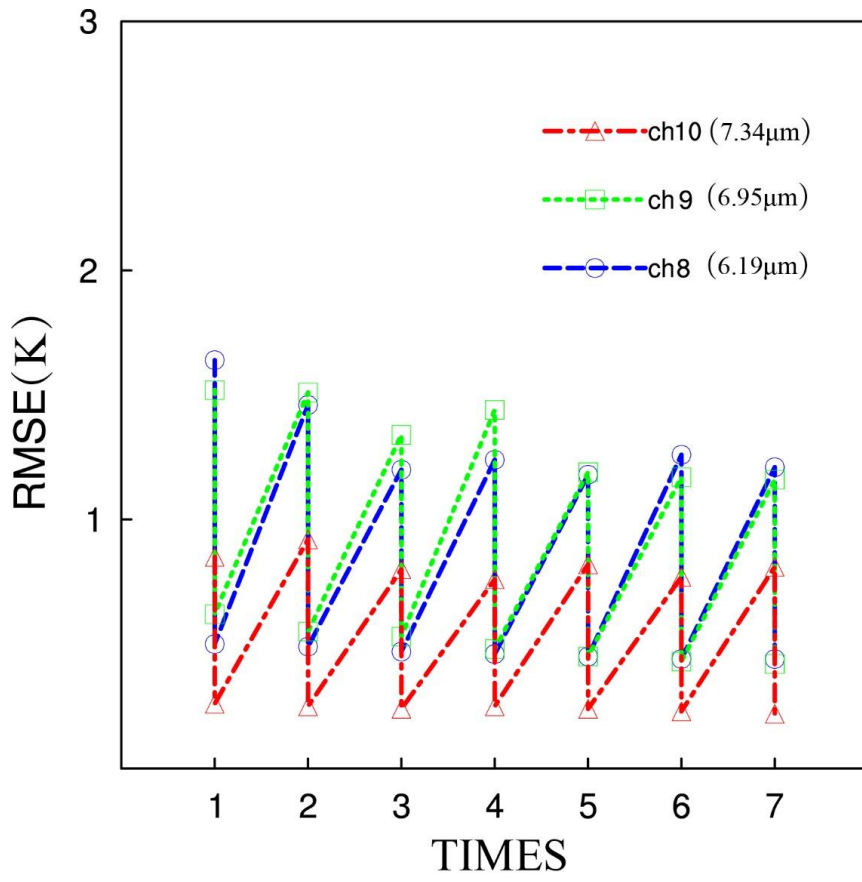
734 Fig. 8 Scatter plots of (a, d and g) the observed and background brightness
 735 temperature before the bias correction of channel 8, 9 and 10. Scatter plots of (b, e
 736 and h) the observed and background brightness temperature after the bias correction
 737 of channel 8, 9 and 10. Scatter plots of (c, f and i) the observed and analyzed
 738 brightness temperature after the bias correction of channel 8, 9 and 10.



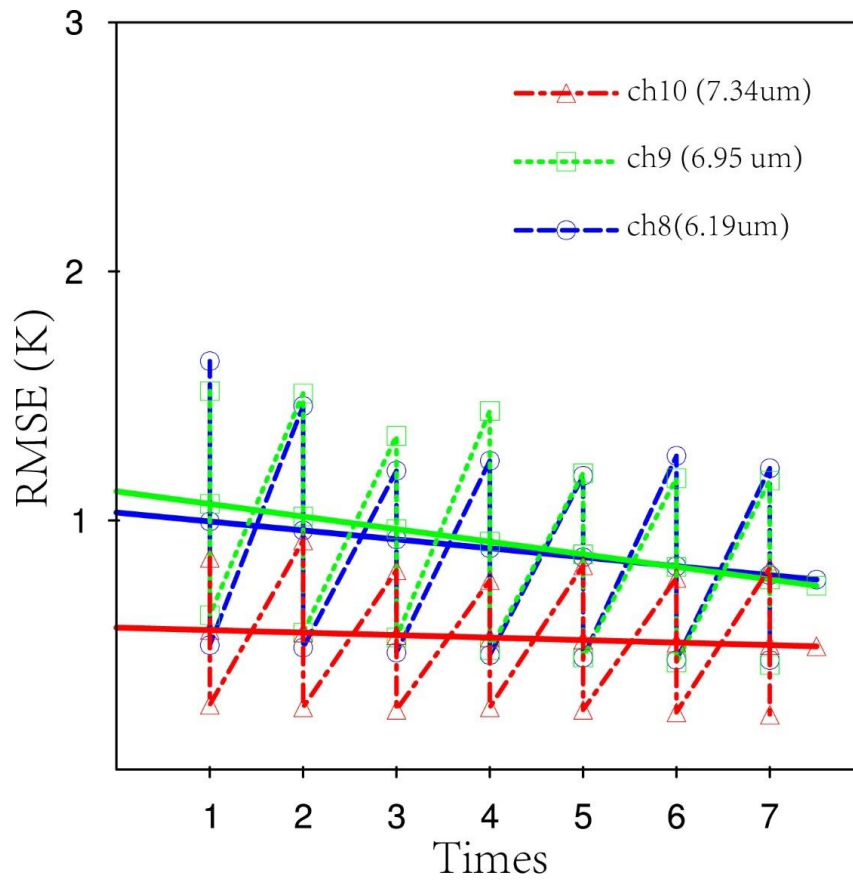
739

740 Fig. 9 Number of (a) observations, (b) mean (unit: K), and (c) standard deviations
 741 (unit: K) of OMB and OMA before and after the bias correction for water vapor
 742 channels 8-10 (OMB_nb: OMB without bias correction; OMB_wb: OMB with bias
 743 correction).

744



745



746

747 Fig.10 Time series of the RMSE for the brightness temperature (unit: K) with
 748 assimilation times before and after the data assimilation along with the trend lines.

749

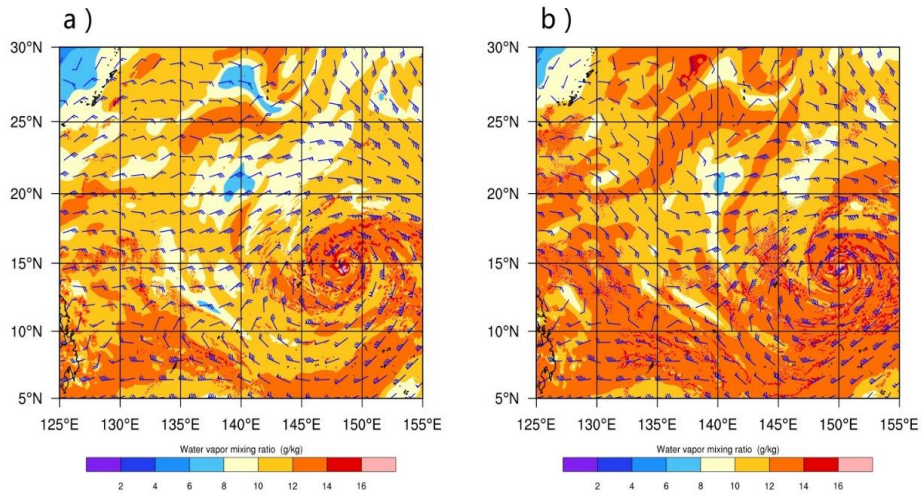
750

751

752

753

754



755

756 Fig. 11 The surface wind speed (vectors, unit: m s^{-1}) and water vapor (colored, unit:
757 g/kg) for (a) CTNL; (b) AHI_DA at 850 hPa at 0000 UTC 2 August 2015.

758

759

760

761

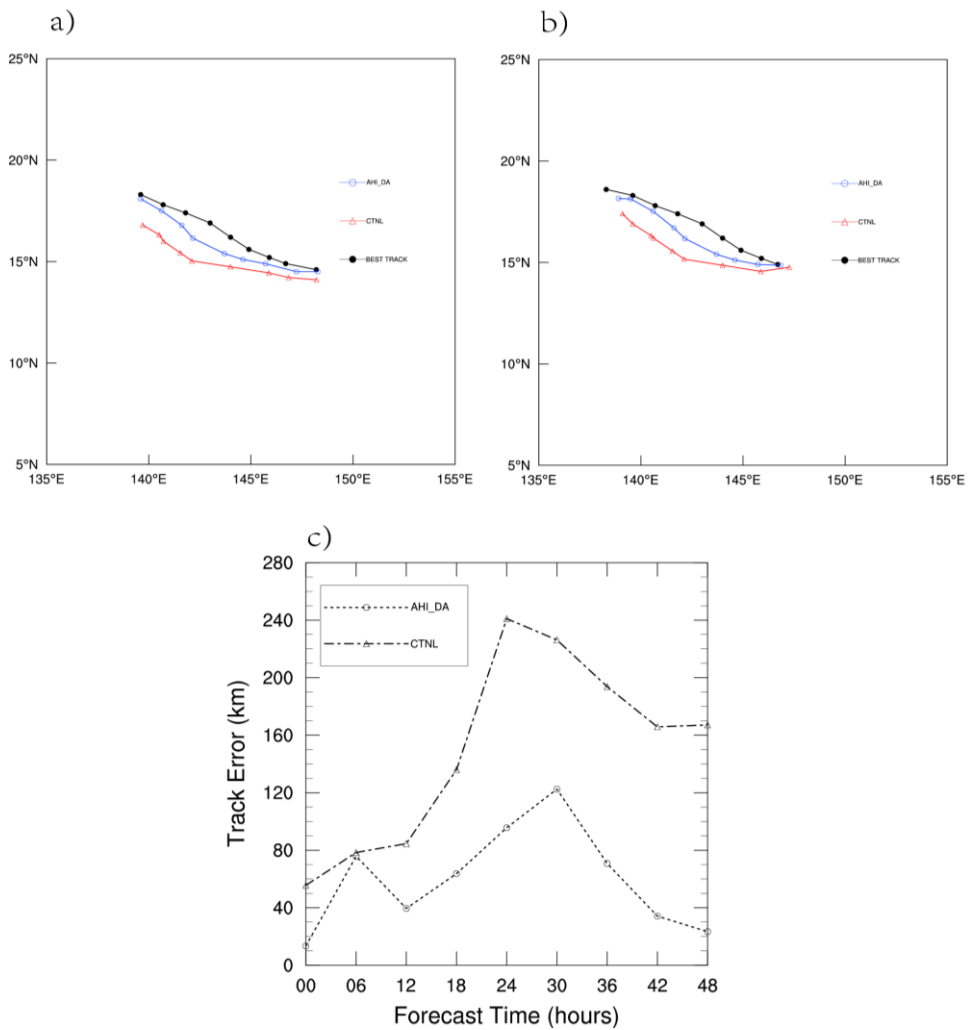
762

763

764

765

766



767

768

769 Fig. 12 The 48-hour predicted tracks (a) from 0000 UTC 2 August to 0000 UTC 4

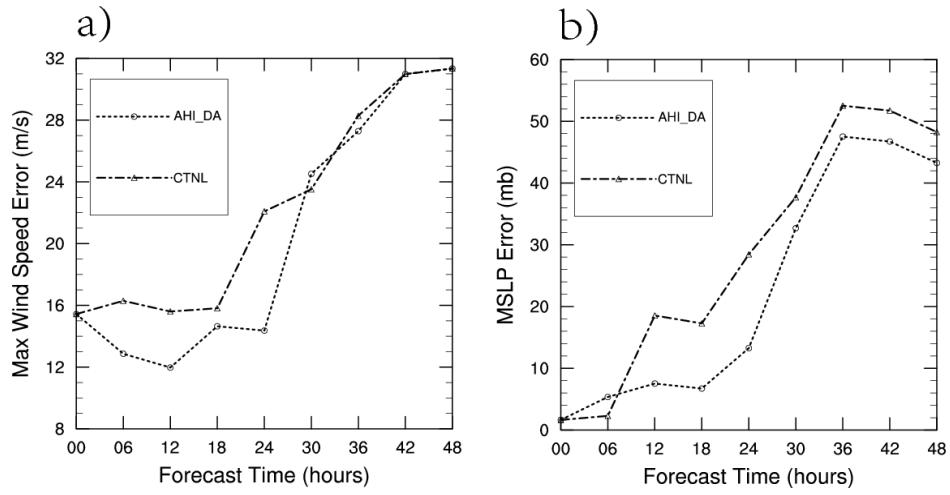
770 August, (b) from 0600 UTC 2 August to 0600 UTC 4 August 2015, (c) averaged track

771 errors (unit: $m\ s^{-1}\ km$) for the two forecasts.

772

773

774



775

776 Fig.13 The 48-hour (a) maximum surface wind [error](#) (unit: m s^{-1}), (b) minimum sea
777 level pressure [error](#) (unit: hPa) of Soude~~lor~~lor [\(2015\)](#) averaged from two forecasts.

778

779

780 **Reply to reviewer 1**

781 Major comment

782 1. A very critical error in title and Fig. 13. “Typhoon Soulder” →”Typhoon Soudelor”, Also,
783 please specify Soudelor’s year for the clarity.

784 -----

785 Reply: Thanks. Corrected as “Fig.13 The 48-hour (a) maximum surface wind (unit: $m s^{-1}$), (b)
786 minimum sea level pressure (unit: hPa) of Soudelor (2015) averaged from two forecasts.”

787

788 2. Line 232: “Grell Devenyi cumulus parameterization scheme (Grell et al., 2002),” By the way, it
789 is not always true. Nevertheless, since the authors set a 5-km spatial resolution in this study, I am
790 very wondering why the authors did activate Grell Devenyi cumulus parameterization?

791 -----

792 Reply: Agreed. In fact, we also conduct sensitivity experiments to turn off the cumulus
793 parameterization for this case. It is found that there is no significant difference between them. The
794 application of Grell Devenyi cumulus parameterization scheme we used in our current study is
795 following that used in Li et al., (2012) with 5-km spatial resolution.

796 Reference:

797 Li, Y., Wang, X., Xue, M., 2012. Assimilation of radar radial velocity data with the WRF
798 ensemble-3DVAR hybrid system for the prediction of hurricane Ike (2008). Mon. Weather
799 Rev. 140, 3507–3524.

800

801 Minor comments

802 1. Lines 59-62: the sentence starts with “some researches ...” but the authors cited one paper”
803 Please cite more papers or revise this sentence.

804 -----

805 Reply: Thanks. Corrected as “Some researches demonstrated that in global model, satellite
806 radiance DA makes more contribution to improving the accuracy of the numerical model results

807 than conventional observation DA does (Zapotocny et al., 2007, Yan et al., 2010; Geer et al.,
808 2017).”

809 Reference added:

810 Geer, A. J., Baordo, F., Bormann, N., English, S., Kazumori, M., Lawrence, H., Lean, P., Lonitz,
811 K., and Lupu, C.: The growing impact of satellite observations sensitive to humidity, cloud
812 and precipitation, *Quart. J. Roy. Meteorol. Soc.*, 143, 3189–3206.

813 Yan, B., F. Weng, and J. Derber (2010), Assimilation of satellite microwave water vapor sounding
814 channel data in NCEP Global Forecast System (GFS), paper presented at 17th International
815 TOVS Study Conference, Int. ATOVS Working Group, Monterrey, Calif.

816

817 2. Lines 68-69: I cannot understand what the authors mean (in bold) “it is highlighted that they are
818 not able to perform continuous monitoring over a fixed area, **thus leaving out some rapidly**
819 **intensified TCs or storms.**”

820 -----

821 Reply: Thanks. The sentence is revised as “However, it is highlighted that they are not able to
822 generate continuous observations for a fixed regional area and so may miss rapidly intensified TCs
823 or storms.”

824

825 3. Line 70: “because geostationary satellites have a fixed location related to the earth’s surface,” it
826 could potentially give a misunderstanding to the reader. Please just say “rotate with the earth”.

827 -----

828 Reply: Agreed. The sentence is revised as “However, it is highlighted that they are not able to
829 generate continuous observations for a fixed regional area and so may miss rapidly intensified TCs
830 or storms. On the contrary, because geostationary satellites rotate with the earth, although their
831 resolutions are lower than that of polar-orbit satellites, they can capture the formation and
832 development of mesoscale convective systems by continuous monitoring (Montmerle et al., 2007;
833 Stengel et al., 2009; Zou et al.,2011).”

834

835 4. Line 76: “In fact, they can capture convective spiral cloud systems relating to TCs.” Since the

836 geostationary satellites can capture more features related to TCs, the authors need to consider
837 make a list or remove this sentence.

838 -----

839 Reply: Agreed. The sentence is removed according to the reviewer's suggestion.

840

841 5. Lines: 236-262: is there any reason why the authors explain first Figs. 5 and 6 and followed by
842 Fig. 4?

843 -----

844 Reply: Figure 4 is firstly explained at line 231 before Figure 5 at line 238 and Figure 6 at line 273.

845

846 Technical comments

847 1. In Abstract, remove JMA WRF-3DVAR abbreviations.

848 -----

849 Reply: Corrected.

850

851 2. Please keep the abbreviation order: some are "Abbreviation (extended)" and some extended
852 form (abbreviation) (Lines: 163-164). Please fix this from the whole manuscript.

853 -----

854 Reply: Agreed. All related sentence is revised as the format of extended (Abbreviation).

855

856 3. Line: 228, Model center is (17.5 °N, 140 °E) (Fig. 4). ?? please make a complete sentence.

857 -----

858 Reply: Agreed. The sentence is completed as "The center of the model domain is located at
859 (17.5 °N, 140 °E) (Fig. 4)."

860

861 Editorial comments

862 1. "the background field of the model is effectively corrected..." → "...was effectively
863 corrected...". Please consider whether the authors want to keep "past form of a verb. In my
864 opinion, if the authors are explaining the results of this work, it should be the past form of a verb.

865 (not critical)

866 -----

867 Reply: Agreed. Following the editor's suggestion, the past form is applied for the whole
868 manuscript.

869

870 2. Lines: 278, 280, "Fig. 7a, c, e" (go through the whole manuscript) → "Figs. 7a, c, and e" .

871 -----

872 Reply: Corrected.

873

874

875 **Reply to reviewer 2**

876 General comments

877 This paper built an interface for AHI radiance data assimilation on the WRFDA system based on
878 the 3DVAR assimilation method. Two experiments for comparison was designed to examine the
879 effect of AHI water vapor channel radiance data assimilation on the analysis and prediction of the
880 rapid intensification period of Typhoon Soudelor in 2015. To some extent, the assimilation of AHI
881 radiance data is able to improve the analyses of the minimum sea level pressure, the maximum
882 surface wind, as well as the typhoon track. The whole developing stages of Typhoon Soudelor
883 including a rapid intensification, a weakening, a second intensification, then a continuous
884 weakening till disappearing. However, only the first intensification during 1 August to 3 August
885 considered as study period seems insufficient to efficiently prove the advantages of AHI radiance
886 data assimilation. According to the comparison of the two experiments during 48 hours
887 forecasting period (Fig.13), the forecast error of AHI_DA model in the first 30 hours is obviously
888 smaller than the CTNL model's result, however in the later 18 hours the forecast error between
889 these two models is quite close. That means the forecasting error could possibly seriously increase
890 for a longer simulation time. Thus in order to more efficiently prove the advantages of AHI
891 radiance data assimilation and promote the contributions of this paper, I suggest this research to
892 extend the study period at least include the first intensification, a weakening, and the second
893 intensification of Typhoon Soudelor. In addition, some unclear and unprecise descriptions need
894 carefully to be addressed. Overall speaking, this paper can be considered for publication however
895 the major revision is necessary.

896 -----

897 [Reply: Thanks for the helpful advice. This study focuses on the impact of the assimilating AHI](#)
898 [radiance on the initialization and prediction of a tropical cyclone case for its rapid intensification](#)
899 [stage from 1800 UTC 1 August 2015 to 0600 UTC 4 August 2015. Similar configuration of the](#)
900 [numerical period is also found in Honda et al., \(2018\) and Minamide and Zhang \(2018\), which](#)

901 only cover the first intensity stage.

902 However, we strongly agree that it is worth investigating the impact of AHI data assimilation on
903 the whole period including the first intensification, a weakening, and the second intensification of
904 Typhoon Soudelor to fully prove the advantages of AHI radiance data assimilation. It can be seen
905 from Figure 3 that to include the first intensification, a weakening, and the second intensification
906 of Typhoon, the numerical period should extend another at least 4 days. The partial cycle DA
907 technique and other data assimilation techniques are required to update the large scale fields after
908 several data assimilation cycles, which is beyond the scope of this study. The idea of fully
909 investigating the impact of AHI data assimilation on the whole period including the first
910 intensification, a weakening, and the second intensification of Typhoon Soudelor is added in the
911 conclusion section as “Although, the whole developing stages of Typhoon Soudelor include a
912 rapid intensification, a weakening, a second intensification, only the first intensification during 1
913 August to 4 August considered as the numerical period. It is worth investigating the impact of AHI
914 data assimilation on the whole period including the first intensification, a weakening, and the
915 second intensification of Typhoon Soudelor to fully prove the advantages of AHI radiance data
916 assimilation.”.

917 **References:**

918 Honda, T., and Coauthors. 2018: Assimilating all-sky himawari-8 satellite infrared radiances: A
919 case of typhoon soudelor (2015). *Mon. Wea. Rev.*, 146, 213–229.

920 Minamide, M., and F. Zhang, 2018: Assimilation of all-sky infrared radiances from himawari-8
921 and impacts of moisture and hydrometer initialization on convection-permitting tropical
922 cyclone prediction. *Mon. Wea. Rev.*, 146, 3241–3258.

923

924 Specific comments

925 1. P. 9, Ln 169-177, please add the references for the procedures for AHI radiance data quality
926 control.

927 -----

928 Reply: Agreed. Added as “Apart from eliminating cloud pixels, other procedures are implemented
929 inside the data assimilation framework for the quality control are as follows. (1) when reading the
930 data, remove the observed outliers with values below 50 K or above 550 K; (2) only the marine
931 observations are applied by removing the observations on the land and the observations over
932 complex surfaces; (3) remove observations when the observation minus the background is larger
933 than 3 times of the observation error; (4) the pixels are removed when the cloud liquid water path
934 calculated by the background field of the numerical model is greater than or equal to 0.2 kg/m²; (5)
935 eliminate the data when the observation minus background is greater than 5 K. These two
936 parameters are used for these radiances on different sensors of various satellites such as AMSU-A,
937 MHS, and the Advanced Microwave Scanning Radiometer 2 (AMSR2) (Wang et al., 2018, Yang
938 et al., 2016).”

939

940 2. P. 9, Ln 182, Np needs a definition.

941 -----

942 Reply: Np is defined in the revised manuscript.

943

944 3. P. 12, Ln 236, why you use 6 hours spin-up time? Please give more explanation.

945 -----

946 Reply: More explanation is added as “The 6-hour spin-up period is commonly applied to initialize
947 the typhoon or hurricane system in the data assimilation experiments, although longer spin-up

948 period is also acceptable to introduce more model errors in the background such as 12-hour or
949 24-hour.”

950

951 4. P. 13, Ln 256-260, please add the sensitivity experiment results or some references.

952 -----

953 Reply: Thanks. Corrected as “Also, sensitivity experiments with 25 km, and 30 km thinning mesh
954 are also conducted with similar results (Wang et al., 2018).”

955

956 5. P. 14, Ln 273, how to tell the gradient in Fig. 6b decreases stably with increasing iterations? It
957 keeps decreasing.

958 -----

959 Reply: Agreed, we have revised it as “Besides, the gradient in Fig. 6b decreases generally with
960 increasing iterations.”

961

962 6. P. 14, Ln 273-276, The exponential decrease of the cost function and the change trend of its
963 gradient indicate that the effectiveness of AHI radiance DA. What’s the optimal value of
964 $\log(\text{gradient})$? How to see the final iterated analytical field is close to the observation?

965 -----

966 Reply: Minimization stops when the norm of the gradient for the cost function is reduced by a
967 factor of 0.01, which is commonly used in data assimilation procedures. Inner minimization stops
968 either when the criterion of the cost function gradient is met or when inner iterations reach 200.
969 Related explanation is added in section 4.1. To verify whether the final iterated analytical field is
970 close to the observation, the observations minus the analyses are provided in section 4.2.

971

972 7. P. 14, Ln 279, what is “analytical brightness temperature”?

973 -----

974 Reply: The phrase is revised as “the simulated brightness temperature from the analyses”

975

976 8. P. 14, Ln 281-284, “It should be pointed that even only parts of the AHI radiance data are

977 applied after quality control in the data assimilation, the radiative transfer model is able to
978 simulate the brightness temperature for all the pixels with the background and the analysis
979 respectively for the verification purpose.” This description is unprecise, at least how much should
980 AHI radiance data be considered?

981 -----

982 Reply: Agreed. Related information is added as “It should be pointed that even only parts of the
983 AHI radiance data (roughly 20000 clear sky pixels of total 50000 pixels for each DA cycle) are
984 applied after quality control in the data assimilation, the radiative transfer model is able to
985 simulate the brightness temperature for all the model grid point with the background and the
986 analysis respectively for the verification purpose.”

987

988 9. P. 15, Ln 309-P. 16, Ln 312, the observed and background brightness temperature for ch8 (a→b)
989 and ch9 (d→e) both have significant improvement after the bias correction. However we can't
990 find the similar trend for ch10, please explain.

991 -----

992 Reply: Related explanation is added as “Among them the RMSEs of channel 10 are smallest
993 compared to those from channels 8 and 9 for the OMB and OMA samples, which is likely related
994 to strict cloud detection scheme for channel 10 with rather lower detecting peak (Wang et al.,
995 2018).”

996

997 10. P. 16, Ln 322-324, why the OMB number keeps the same with or without bias correction in
998 Fig. 9(a)? As well as the Stdv (K) of OMB almost keeps the same with or without bias correction
999 in Fig. 9(c).

1000 -----

1001 Reply: Since the bias correction scheme is applied to all the AHI data after quality control, the
1002 OMB number keeps same with or without the bias correction procedure. The standard deviations
1003 (stdv) of OMB were comparable before and after the bias correction, since they are calculated by
1004 subtracting the mean of the bias. It is found that the bias was corrected effectively with an overall
1005 same magnitude of bias for each pixel, leading the stdv almost same before and after the bias

1006 correction. Related explanation is added in section 4.2 at line 348.

1007

1008 11. P. 17, Ln 351-352, after the assimilation of AHI radiance data, except the streamlines in the
1009 typhoon region become denser, the upper left region somehow showed quite different streamline
1010 pattern. Is this also part of improvements?

1011 -----

1012 Reply: The field outside of the typhoon center is also modified with the data assimilation of AHI
1013 radiance data to provide a favorable environment field for a developing vortex. The related
1014 explanation is added as “This suggests that the field outside of the typhoon center is also adjusted
1015 as the assimilation of AHI radiance data was able to improve the large-scale environmental field
1016 in the simulation region of Typhoon Soudelor.”

1017

1018 12. P. 19, Ln 379-380, “the track predicted by AHI_DA match better with the best track”. This
1019 description is unprecise, only better match at the start point and the end point. There still have not
1020 small track error during the middle region.

1021 -----

1022 Reply: Agreed. The improvement is most obvious at the start and end point. From both the
1023 48-hour predicted tracks from 0000 UTC 2 August (Fig. 12a) and from 0600 UTC 2 August (Fig.
1024 12b), the typhoon track predicted by the CTNL continues to show a south-west bias (the red track),
1025 while the track predicted by AHI_DA (the blue track) match better with the best track (the black
1026 track). The sentences are revised as “The improvement is most obvious at the start and end point.
1027 As can be seen in Fig. 12a, at the beginning of the forecast, the initial location of the typhoon from
1028 the CTNL experiment has large south bias and east bias at 0000 UTC and 0600 UTC respectively.
1029 Conversely, the location of the typhoon in AHI_DA is relatively closer to the observation at the
1030 beginning.”

1031

1032 13. P. 19, Ln 392-393, “It can be seen that the maximum surface wind error predicted by the
1033 AHI_DA is much lower than that by the CTNL..”, This description is only valid before 30 hours
1034 of forecast time, but after 30 hours both models show similar error degree.

1035 -----

1036 Reply: The statements are modified as “It can be seen that the maximum surface wind error
1037 predicted by the AHI_DA was much lower than that by the CTNL for the first 30 hours, due to the
1038 overall under estimation for the intensity of Typhoon Soudelor simulated in the background field.
1039 The maximum surface wind errors of AHI_DA are generally smaller than those of CTNL. It
1040 should be pointed out that the difference between the maximum surface wind errors of the two
1041 experiments reaches up to 7.5 m s⁻¹ after 24-hour forecast. In Fig. 13b, the results of the minimum
1042 sea level pressure are consistent with Fig. 13a, while the improvement for the minimum sea level
1043 pressure lasts for 40 hours.”

1044

1045 14. P. 20, Ln 395-396, “The maximum surface wind predicted by AHI_DA fit closer to the best
1046 track data with the maximum difference about 2.6 m/s after 12 hours forecast”. This description
1047 seems not matching with Fig.13(a).

1048 -----

1049 Reply: Agreed. Sorry for the typo we made. The sentence is revised as “The maximum surface
1050 wind errors of AHI_DA are generally smaller than those of CTNL. It should be pointed out that
1051 the difference between the maximum surface wind errors of the two experiments reaches up to 7.5
1052 m s⁻¹ after 24-hour forecast.”

1053

1054 15. P. 21, Ln 416-418, conclusion 3 “It is found that the track, maximum surface wind, and
1055 minimum sea level pressure from the AHI radiance data assimilation experiment match better with
1056 the best track than the control experiment does for the subsequent 18-hour forecast”. This
1057 conclusion doesn’t match with the findings from Fig.12 and Fig.13.

1058 -----

1059 Reply: The sentence is corrected as “Generally, the track and minimum sea level pressure from the
1060 AHI radiance data assimilation experiment match better with the best track than the control
1061 experiment does for the subsequent 48-hour forecast. The maximum surface wind forecast error is
1062 reduced only for the first 30-hour.”

1063

1064 16. P. 31, Fig.3, the legend is wrong. The dash line should be maximum surface wind and the solid
1065 line should be minimum sea level pressure.

1066 -----

1067 Reply: Thanks. Fig. 3 is replotted.

1068

1069 17. P. 32, Fig.4, what the different symbols (triangle and circle) represent?

1070 -----

1071 Reply: Agreed. To make it clear, a sentence is added as “Each observation type is marked with
1072 different color along with a unique symbol.”

1073

1074 18. P. 38, Fig.10, please add the trend line for each channel in order for better comparison.

1075 -----

1076 Reply: Agreed. The trend lines are added in the revised manuscript.

1077

1078 19. P. 40, Fig.12, the unit of track error (m s-1) in the figure caption is wrong, it should be “km”.

1079 -----

1080 Reply: Thanks. The unit is corrected as km.

1081

1082 20. P. 41, Fig.13, the figure caption should bemaximum surface wind “error” (unit: m
1083 s-1).....minimum sea level pressure “error” (unit: hpa). In addition, the typhoon name “Soudelor”
1084 is misspelled as “Soulder”.

1085 -----

1086 Reply: The caption is revised according to the reviewer as “The 48-hour (a) maximum surface
1087 wind error (unit: m s-1), (b) minimum sea level pressure error (unit: hPa) of Soudelor (2015)
1088 averaged from two forecasts.”

1089

1090 Technical corrections

1091 1. P. 1, Ln 2, the typhoon name “Soudelor” was misspelled as “Soulder” in the paper title.

1092 -----

1093 [Reply: Corrected.](#)

1094

1095 2. P. 6, Ln 110, “weather” forecast.

1096 -----

1097 [Reply: Corrected as weather forecast.](#)

1098

1099 3. P. 3, Ln 57, the cited reference “Pennie, 2010” is not listed in the references.

1100 -----

1101 [Reply: The reference of Pennie, 2010 is deleted in the revised manuscript.](#)

1102

1103 4. P. 25, Ln 515, this reference is not cited in the article.

1104 -----

1105 [Reply: The reference is deleted.](#)

1106

1107 5. P. 26, Ln 523, this reference is not cited in the article.

1108 -----

1109 [Reply: The reference is deleted.](#)

1110

1111

1112 **Reply to reviewer 3**

1113 1. The aim of this topic is Typhoon Soudelor (2015), but the title of this paper is miss-typed.

1114 -----

1115 **Reply: Corrected.**

1116

1117 2. The time notation of Fig. 3 should be more clear as mentioned at line 213.

1118 -----

1119 **Reply: Fig.3 is modified for the time notation for the X axis. The caption is revised to make it**
1120 **more clear as “Fig. 3 The time series of the minimum sea level pressure (solid line, unit: hPa) and**
1121 **the maximum surface wind (dash line, unit: m s-1) of Typhoon Soudelor from the CMA best-track**
1122 **data from 0000 UTC 30 July 2015 to 0600 UTC 12 August 2015. The specific period for the**
1123 **numerical results from 1800 UTC 1 August 2015 to 0000 UTC 3 August 2015 is highlighted in**
1124 **blue.”**

1125

1126 3. The main calculations (key features) of this paper are from line 170 to 177. The authors
1127 should provide more information about the decision of these parameters adopted. Moreover,
1128 the methodology is proposed by the authors or function of this code or processing chain.

1129 -----

1130 **Reply: For the quality control, we follow studies on the direct assimilation of radiance to exclude**
1131 **the useless brightness temperature. These parameters are used for these radiances on different**
1132 **sensors of various satellites such as Advance Microwave Sounding Unit-A (AMSU-A),**
1133 **Microwave Humidity Sounder (MHS), and the Advanced Microwave Scanning Radiometer 2**
1134 **(AMSR2). These thresholds are implant to this GMI DA research to safely remove data, since**
1135 **these data are not able to provide useful information. The manuscript is revised as “Apart from**

1136 eliminating cloud pixels, other procedures are implemented inside the data assimilation framework
1137 for the quality control are as follows. (1) when reading the data, remove the observed outliers with
1138 values below 50 K or above 550 K; (2) only the marine observations are applied by removing the
1139 observations on the land and the observations over complex surfaces; (3) remove observations
1140 when the observation minus the background is larger than 3 times of the observation error; (4) the
1141 pixels are removed when the cloud liquid water path calculated by the background field of the
1142 numerical model is greater than or equal to 0.2 kg/m²; (5) eliminate the data when the observation
1143 minus background is greater than 5 K. These two parameters are used for these radiances on
1144 different sensors of various satellites such as AMSUA, MHS, and AMSR2 (Wang et al., 2018,
1145 Yang et al., 2016). ”

1146
1147 4. The calculation requires iteration but the result presents forecast of typhoon data. Thus the CPU
1148 hours should be provided.

1149 | -----

1150 Reply: The wall clock times used by CTNL and AHI_DA for the data assimilation procedures are
1151 rather comparable with roughly 30 minutes and 40 minutes on a Linux workstation with 36
1152 processors. It should be pointed out that computational cost of the deterministic forecast and the
1153 pre-process for gridded GFS data are same in these two experiments. Related information is added
1154 in the revised manuscript in section 4.1.

1155

1156

1157

1158

1159

1160

1161

1162

1163

1164